IEEE Access
Multidisciplinary | Rapid Review | Open Access Journal

Received 8 November 2022, accepted 1 December 2022, date of publication 5 December 2022, date of current version 8 December 2022.

Digital Object Identifier 10.1109/ACCESS.2022.3226779

RESEARCH ARTICLE

Battery Energy Storage System With Interleaving Structure of Dual-Active-Bridge Converter and Non-Isolated DC-to-DC Converter With Wide Input and Output Voltage

SUNG-JUN PARK[1], JIN WOOK PARK[1], KUK HYEON KIM[1], AND FEEL-SOON KANG[2], (Member, IEEE)

[1]Department of Electrical Engineering, Chonnam National University, Gwangju 61186, South Korea
[2]Department of Mechatronics Engineering, Gyeongsang National University, Jinju 52725, South Korea

Corresponding author: Feel-Soon Kang (feelsoon@gnu.ac.kr)

This work was supported by the Gwangju.Jeonnam local Energy Cluster Manpower training of the Korea Institute of Energy Technology Evaluation and Planning (KETEP) grant funded by the Korea Government Ministry of Knowledge Economy (No. 20214000000560).

ABSTRACT We propose a circuit topology suitable as a battery charge/discharge tester with a DAB converter and a non-isolated dc-dc converter as a module structure. The module structure can be configured to have a wide input and output voltage range because it is easy to expand. DAB converters are used for bidirectional power transfer and galvanic isolation. By controlling the phase difference of the voltages across the DAB to be almost identical, the generation of circulating current due to the phase difference is minimized, and the ZVS is guaranteed. In addition, by switching at a phase angle that flattens the DAB switch current, the peak current is reduced to diminish the switch's conduction loss, lowering the switch current rating, and reducing the magnetic core size. The non-isolated dc-dc converter is used to control the battery output voltage. Through the interleaved structure, good dynamic characteristics and current ripple can be reduced, so the effect of improving the battery lifecycle can be expected. We present four series-parallel structures of the proposed converter and compare them with the case of generating an output voltage only with a DAB converter. Analyze the characteristics of automatic voltage balancing due to the difference between the input capacitors' initial voltage and capacitance connected in series. We analyze the features of the proposed system through simulation and verify the technical feasibility and excellence of the proposed battery charge/discharge tester through charge/discharge experiments using supercapacitors instead of batteries.

INDEX TERMS Battery charge/discharge tester, converters, dual active bridge (DAB), input-series and output-parallel (ISOP), interleaved, non-isolated, zero-voltage switching (ZVS).

I. INTRODUCTION

High-voltage DC transmission systems are widely used in rail transport systems, electric vehicle battery charging systems, and DC grids [1]. In these applications, DC supply voltages can reach up to several kilovolts, which is often difficult to construct using a single power semiconductor. To solve this problem, a modular approach is applied to improve output performance, such as increasing voltage and current levels handled by power converters, improving efficiency, reducing costs, and reducing output ripple [3], [4], [5], [6], [7], [8], [9]. Among them, input-series and output-parallel (ISOP) connected modular dc-to-dc converters enable the optimization of high input voltage and high output current converters [4], [6], [7], [8], [10], [11]. In general, DAB (dual active bridge) is more suitable for high-power applications

The associate editor coordinating the review of this manuscript and approving it for publication was Zhehan Yi.

with high efficiency, bidirectional operation, and fault isolation compared to other isolated dc-to-dc converters [12], [13], [14] and is used for applications such as high and medium power [14], [15], [16], [17], [18], [19], [20], [21], [22], [23], [24], [25], [26], [27]. The control of the modular structure must ensure proper voltage and current distribution between modules to achieve safe and suitable operation [4], [6], [9], [10]. For ISOP connections, each module's input voltage and output current must be kept within acceptable ranges, ideally the same value for all modules. The output voltage must also be adjusted [11]. The most straightforward power balance control strategy is to use an output voltage regulator (OVR) to regulate the transferring power of all modules [29], [30]. However, due to the inevitable mismatch of parameters between modules, transmit power balancing cannot be achieved with OVR alone. Many control methods of ISOP dc-to-dc converters, including distributed control strategies and master-slave control strategies, can accomplish the transmit power balancing of DAB ISOP dc-to-dc converters. Distributed control strategies such as input voltage droop control and output current reverse droop control based on positive output voltage slope have the advantage of no control interconnection between modules and a simple structure [31], [32], [33], [34]. Still, on the other hand, there are many limitations and poor dynamic and steady-state properties [35], [36]. In addition, the transfer current of the DAB dc-to-dc converter includes alternating current, so transfer current-based control is not suitable. Above all, droop-based control schemes generally have poor dynamic and steady-state performance [37]. Furthermore, since the PI controller that regulates the input voltages of both modules is used to determine the phase shift ratio, not the delivered power, it also affects the output voltage. These existing studies focus more on power-sharing performance. They have not conducted studies on the disturbance of input voltage and load current by the fast dynamic response of the ISOP DAB dc-to-dc converter [12].

This paper, rather than solving the ISOP problem through the control method, solves the problem through the combined topology using DAB and the non-isolated converter. Through simple control of DAB and output power control of non-isolated converter, we propose a topology that is effective for fast dynamic characteristics and load fluctuations and is used for battery charge/discharge tester. First, the operation of the DAB converter and the interleaved non-isolated dc-to-dc converter constituting the proposed converter are analyzed. The proposed converter has a modular structure and can be applied to a wide voltage range through serial/parallel connection of input/output terminals. By minimizing the phase difference between the voltages on both sides of the DAB converter, the circulating current due to the phase difference is minimized. The current peak is reduced by setting the switching angle to flatten the DAB switch current. Therefore, the loss due to the generation of reactive power is slight, and the current peak is low, which has the advantage of lowering the switch rating and reducing the core size of the magnetic component. In addition, controlling the output voltage through an interleaved non-isolated dc-to-dc converter reduces current ripple and has fast response characteristics. To prove the technical feasibility and superiority of the proposed converter structure, automatic voltage balancing by the initial voltage difference and capacitance difference for the input capacitors connected in series is analyzed. The design procedure to obtain the critical design parameters of the proposed converter is presented, and its validity is verified through simulation and experimentation. We measure the efficiency when operating the four series-parallel structures that the proposed converter can implement at 50V, 100V, and 150V and compare it with the case of generating an output with only a DAB converter.

II. REVIEW OF HIGH-FREQUENCY ISOLATED BIDIRECTIONAL DC-DC CONVERTERS SUITABLE FOR BATTERY CHARGE/DISCHARGE TESTER

A converter capable of bidirectional power transfer and galvanic isolation between the grid and the battery is required for ESS (Energy Storage System) and battery charge/discharge tester applications.

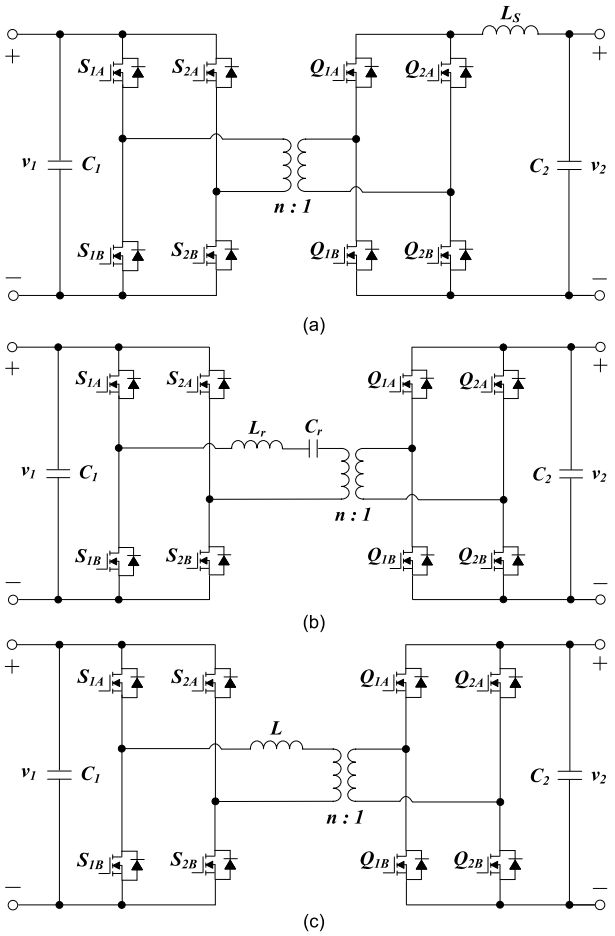

FIGURE 1. Bidirectional isolated dc-to-dc converter suitable for a battery charge/discharge tester, (a) phase-shifted full-bridge (PSFB) converter, (b) resonant dual active bridge (DAB) converter, (c) DAB converter.

Generally, a transformer is used to insulate the grid and the battery. The use of a low-frequency transformer has

the disadvantage of increasing the volume of the transformer. Recently, an isolated dc-to-dc converter using a high-frequency transformer has been mainly used. This chapter analyzes and summarizes the characteristics of a high-frequency isolated bidirectional dc-to-dc converter suitable for a battery charge/discharge tester [1]. Fig. 1 shows a representative bidirectional isolated dc-to-dc converter suitable for battery charge/discharge testers; Phase shifted full-bridge (PSFB) converter, resonant dual active bridge (DAB) converter, and DAB converter. These converters have an active switch-based bridge circuit and a high-frequency transformer in common at both [38], [39].

A. PHASE SHIFTED FULL-BRIDGE (PSFB) CONVERTER

The PSFB converter given in Fig. 1(a) has the same circuit structure as the most basic isolated full-bridge dc-to-dc converter. A phase shift method is selected to improve the characteristics of ZVS. The transformer's primary is connected through a capacitor to show the features of the voltage source, and the secondary shows the characteristics of the current source due to the dc inductor for the filter. A high-frequency transformer provides galvanic isolation and adjusts the voltage gain. $V_2/V_1 = ND$ if the transformer turns ratio is N when the duty ratio D determines the voltage gain. Therefore, the PSFB converter voltage gain is limited to a maximum of N. A dc inductor is additionally connected to reduce the output ripple, and a relatively larger inductance is required compared to other converters, so the price increase and power density decrease. To ensure the ZVS, the transformer must have a leakage inductance above a certain level. However, the usable duty ratio range is limited due to the influence of the inductance, thus limiting the voltage gain. In addition, since switching occurs between the leakage inductance of the transformer and the dc inductor of the output stage, there is a problem with generating a voltage spike in the secondary switch due to the current difference between the two inductors [40], [41], [42], [43].

B. RESONANT DUAL ACTIVE BRIDGE CONVERTER

Fig. 1(b) is the resonant bridge converter's most widely used LLC-type converter. The series resonant converter has a limited voltage gain. The parallel resonant converter has a disadvantage in that the conduction loss due to the circulating current is significant at a light load. The resonant dc-to-dc DAB converter was introduced to solve the shortcomings of the existing series resonant and parallel resonant dc-to-dc converters. Since the voltage gain-frequency characteristic is steep near the resonance point, there is an advantage that it can be controlled only with a relatively small frequency change in a wide voltage range. However, the asymmetric circuit structure differs between forward and reverse operation characteristics. In particular, in the case of reverse control, the voltage gain width is limited because it operates in the same way as the existing series resonant converter. Because it is controlled at a variable frequency, it is not easy to optimize the converter design. Additional components are required for resonance, and the inductance needed for resonance is designed to be larger than the inductance used in the DAB converter. It is also difficult to optimize the power density because a capacitor for resonance is also required [44], [45], [46].

C. DUAL ACTIVE BRIDGE CONVERTER

The advantage of DAB converters given in Fig. 1(c) is that they can be electrically isolated and transfer power in both directions with only a small number of devices. In a DAB converter, power transfer is only through an inductor connected to the transformer. The series inductance may use an additional inductor or a transformer's leakage inductance. In addition, since the inductor of the DAB converter operates as an AC inductor, the same power delivery is possible with a much smaller inductance than the PSFB converter. Therefore, when both ends of the transformer are configured as a bridge circuit, there is no need for additional passive components, which is very useful for increasing power density. The inductor current waveform is determined by the voltage applied across the DAB converter. Therefore, since the inductor current has a lagging phase compared to the primary voltage and a leading phase compared to the secondary voltage, ZVS operation of all switches is possible in a wide range. The most basic control method of the DAB converter is to control only the phase difference between the primary and the secondary voltage. However, as the voltage ratio changes and drops to a light load, the ZVS characteristic deteriorates, and the circulating current increases, so the conversion efficiency decreases rapidly. Also, since the input and output of the DAB converter are both configured as voltage sources, the input and output capacitors have to filter the AC current, so the capacitor has to filter the high RMS current [47], [48], [49], [50].

III. PROPOSED CONVERTER STRUCTURE SUITABLE FOR BATTERY CHARGE/DISCHARGE TESTER

It can be seen that the overall system performance is improved by minimizing the current stress of the converter switch [51], [52], [53], [54], [55], [56], [57], [58], [59], [60], [61]. Reducing the current stress decreases the switch current rating and the volume and loss of magnetic components. In addition, the conduction loss and switching loss of the converter can be reduced, which helps to improve the system's efficiency.

Fig. 2 shows the proposed circuit configuration. DAB converter and non-isolated dc-to-dc converter are combined. Two DAB converters are coupled in parallel, and four non-isolated converters are connected in parallel. The input stage is connected in series to obtain a wide range of input voltage. The basic module of the proposed converter minimizes reactive power generation due to circulating current by maintaining almost no voltage phase difference between both sides of the DAB. It can overcome the limitations of the existing phase-shifted modulation (PSM) by using an interleaved structure that combines a non-isolated dc-to-dc converter for output control. In the case of the existing DAB converter, current

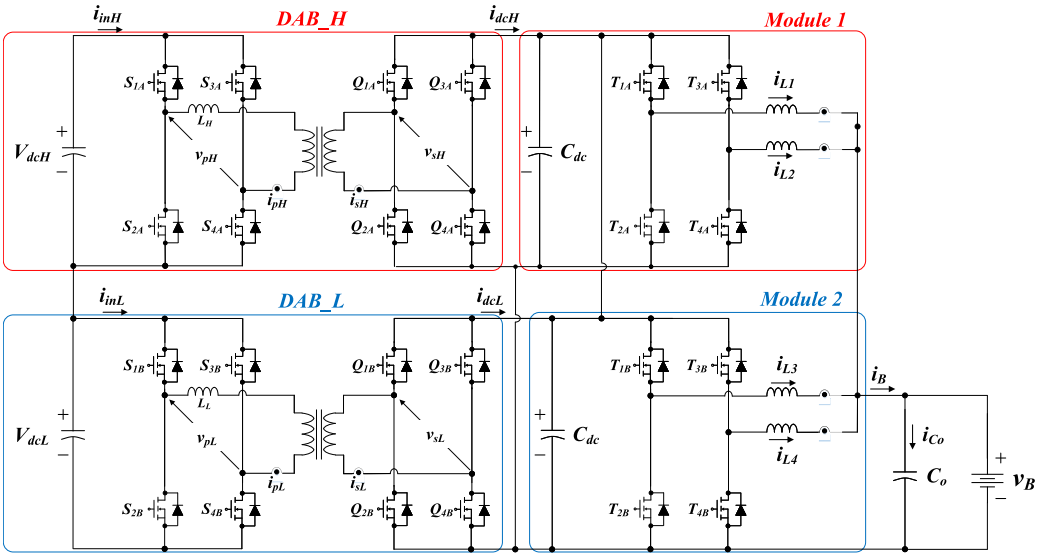

FIGURE 2. The proposed converter structure in which two DAB converters are combined in parallel and four non-isolated dc-to-dc converters are interleaved at the output stage.

stress reduction and ZVS were achieved through a complex control at light load or when the voltage ratio was not 1:1. On the other hand, in this paper, a battery charge/discharge tester with reduced current stress and fast response is realized by utilizing the interleaved structure with the parallel combination of two DAB units and four non-isolated converters.

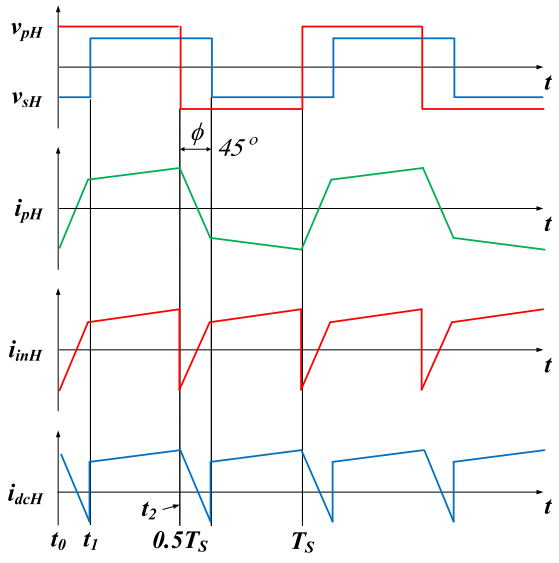

FIGURE 3. When the phase difference between the voltages across the DAB is 45 degrees in the SPS modulation, the primary voltage, secondary voltage, inductor current, primary current, and secondary current are in order from the top.

A. STEADY-STATE ANALYSIS OF DAB CONVERTER CONTROLLED BY PHASE-SHIFT MODULATION

This chapter reviews the case where the DAB converter is controlled by the single-phase shift (SPS) modulation method under steady-state conditions. The most basic driving method of the DAB converter is the single-phase shift (SPS) modulation, which applies V_P and V_S as square waves and controls using the phase difference between the two voltages. Fig. 3 shows the primary voltage, secondary voltage, inductor current, primary current, and secondary current when the phase difference is 45 degrees during two cycles. The PSM method performs two operational modes during one cycle according to the phase state of the two voltages [47].

$$i_{pH}(t_1) = i_{pH}(t_0) + \frac{1}{L_H}\left(v_{pH} + nv_{sH}\right)(t - t_0) \quad (1)$$

$$i_{pH}(t_2) = i_{pH}(t_1) + \frac{1}{L_H}\left(v_{pH} - nv_{sH}\right)(t - t_1) \quad (2)$$

Since v_{pH} and v_{sH} are in a steady state, the average value of the current flowing through the inductor is 0. Therefore, we can obtain the following boundary conditions.

$$i_{pH}(t_0) = -i_{pH}(t_2) \quad (3)$$

Substituting (1) and (2) into (3) to calculate the inductor current at t_2 is as follows.

$$i_{pH}(t_2) = \frac{T_s}{2L_H}\left[\frac{1}{2}v_{pH} + \left(\frac{\phi}{\pi} - \frac{1}{2}\right)nv_{sH}\right]$$
$$where\ \ t_1 - t_0 = \left(\frac{\phi}{2\pi}\right)T_s, \quad t_2 - t_1 = \left(1 - \frac{\phi}{2\pi}\right)T_s \quad (4)$$

The input current (i_{inH}) of the DAB converter is determined by the switching state of the primary and secondary and the condition of the inductor current. The average value of the input current is the same as (5).

$$\langle i_{inH}\rangle = \frac{v_{sH}}{L_H f_s} \cdot \frac{\phi}{2\pi}\left(1 - \frac{\phi}{\pi}\right) \quad (5)$$

Therefore, assuming that the converter is ideal, calculating the average power of the converter using the average input

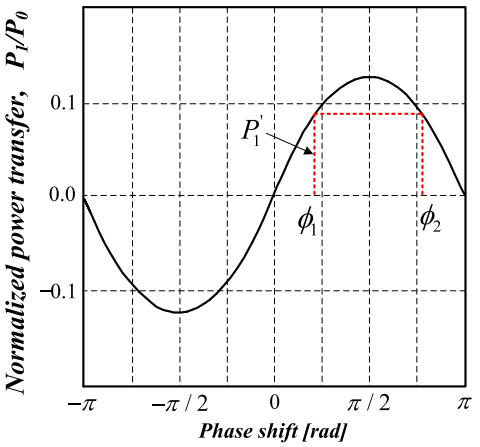

FIGURE 4. Transfer power of DAB Converter by single phase shifted (SPS) modulation.

current becomes (6).

$$P_{1H} = P_{2H} = \frac{nv_{pH}v_{sH}}{L_H f_s} \cdot \frac{\phi}{2\pi}\left(1 - \frac{|\phi|}{\pi}\right) \tag{6}$$

Fig. 4 shows the power by (6) when the phase difference ϕ varies from $-\pi$ to π. If the magnitude of the power is normalized to the standard power P_0, it is equal to (7).

$$P_0 = \frac{nv_{pH}v_{sH}}{L_H f_s} \tag{7}$$

When the phase difference is greater than 0, since the primary voltage leads to the secondary voltage, power is transferred from the input to the output. On the other hand, when the phase is less than zero, the primary voltage lags behind the secondary voltage, and the power transfer direction is reversed. In Fig. 4, the phase value that can transmit an arbitrary amount of power P'_1 is obtained from two operating points, ϕ_1 and ϕ_2. However, if a certain ϕ is minor than $-\pi/2$ or larger than $\pi/2$, the phase difference between the full bridge voltage and the current is significant, causing a circulating current. The maximum power transfer condition of the DAB converter is when the input/output voltage and the inductor are constant when ϕ is $\pm\pi/2$. As for the magnitude of the maximum power, when the magnitude of the DC voltage and the switching frequency of both ends are fixed in (6), the smaller the value of the series reactance of the transformer element, the greater the current flowing.

B. BIDIRECTIONAL NON-ISOLATED CONVERTER

This chapter describes the non-isolated dc-to-dc converter for battery charging and discharging on the output side. Fig. 5 shows only the non-isolated dc-to-dc converter among the overall system diagram of Fig. 2. It adopts an interleaved method that consists of two modules (4 in parallel) of a Buck-Boost converter. This modular method is a structure in which power capacity can be expanded through additional series-parallel coupling. In addition, since the interleaved method increases the switching frequency by the number of interleaved, there is an advantage in that the device rating and size of the inductor and capacitor are reduced, and the current ripple is reduced.

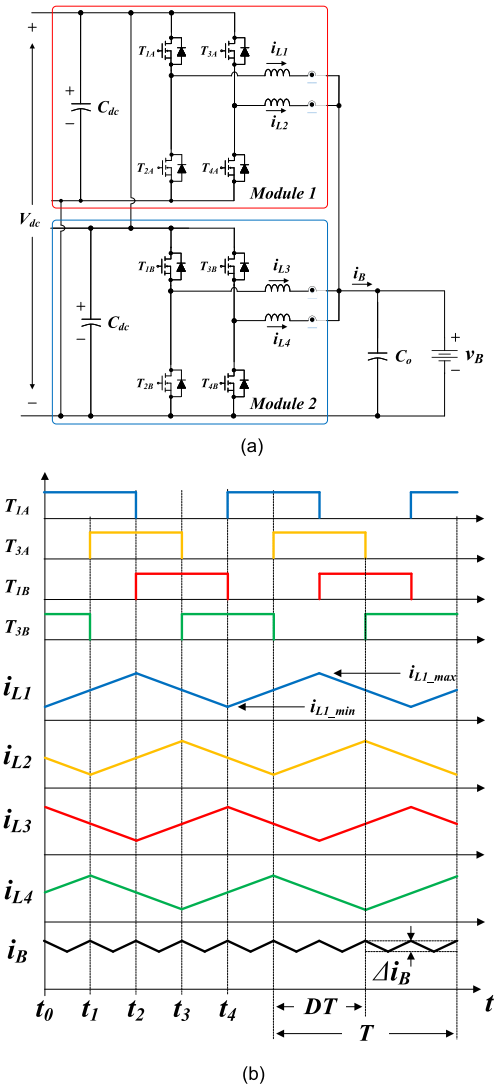

FIGURE 5. Interleaving structure and operation of non-isolated dc-to-dc converter for battery charging and discharging, (a) circuit configuration of the interleaved non-isolated converters, (b) key waveforms at step-down operation.

In the interleaved structure, the number of inductors and switches is required as much as the number of phases (N), and the battery charging current i_B flows through each phase divided by $1/N$ times. In Fig. 5(b), each phase's inductor current (i_{Lx}, x=1,2,3,4) has a phase difference of $2\pi/N$, that is, $360/N$ degrees. The slope of the inductor current is as follows.

$$\frac{di_{Lxon}}{dt} = \frac{v_B}{L_x} \tag{8}$$

$$\frac{di_{Lxoff}}{dt} = \frac{v_B - V_{dc}}{L_x} = \frac{D}{(1-D)}\frac{v_B}{L_x} \tag{9}$$

Here, i_{Lxon} is the inductor current in the rising section, and i_{Lxoff} is the inductor current in the falling area. Therefore, the

current ripple for one phase is defined as (10).

$$\Delta i_B = \frac{v_B}{L} DT \tag{10}$$

The converter's input current is represented by the sum of the inductor currents in each phase.

$$i_B = \sum_{k=1}^{n} i_{L_k} \tag{11}$$

Since the inductor currents of each phase cross and cancel each other, the battery charging current ripple is reduced by at least 1/N times compared to a single phase, and the period becomes T/N. The ripple frequency of the charging current increases by N times the inductor current. The ripple of the battery charging current can be expressed as (12).

$$\frac{di_B}{dt} = (N_{on} + 1)\frac{di_{L_{xon}}}{dt} + N_{off}\frac{di_{L_{xoff}}}{dt} \tag{12}$$

Here, N_{on} denotes the number of switches that maintain an ON state during the T period of the input current, and N_{off} denotes the number of switches that maintain an OFF state. By substituting (8) and (9) into (12), the result is as follows.

$$\frac{di_B}{dt} = \left(\frac{1-d}{1-D}\right) \cdot \frac{v_B}{L_x} \tag{13}$$

$$\Delta i_B = N \cdot \frac{v_B}{L_x} \cdot \left(\frac{1-d}{1-D}\right) \cdot dT \tag{14}$$

Here, N is the number of phases, and d is the ratio of the rising section of the input current. The current ripple of the non-isolated converter of the proposed interleaved method is summarized according to the duty ratio as follows.

$$\Delta i_B = \frac{v_B}{L_x} \cdot \left(\frac{1-4D}{1-D}\right) \cdot \frac{T}{N} \cdot d, \quad 0 < D < 0.25 \tag{15}$$

$$\Delta i_B = \frac{v_B}{L_x} \cdot \left(\frac{2-4D}{1-D}\right) \cdot \frac{T}{N} \cdot d, \quad 0.25 < D < 0.5 \tag{16}$$

$$\Delta i_B = \frac{v_B}{L_x} \cdot \left(\frac{3-4D}{1-D}\right) \cdot \frac{T}{N} \cdot d, \quad 0.5 < D < 0.75 \tag{17}$$

$$\Delta i_B = \frac{v_B}{L_x} \cdot 4 \cdot \frac{T}{N} \cdot d, \quad 0.75 < D < 1 \tag{18}$$

$$where \;\; d = N \cdot D - N_{on}$$

The reduction of capacitor voltage ripple due to the battery charging current ripple reduction can be obtained by using the average charge Q of the capacitor in Fig. 6.

$$Q = \left(N_{off} + 1\right) I_{Lx} - \frac{V_B}{R}(1-d)\,\tau = \frac{V_B}{R} \cdot \frac{d}{N^2} \cdot \left(\frac{1-d}{1-D}\right) \cdot T \tag{19}$$

Therefore, the capacitor voltage ripple is as follows.

$$\Delta v_B = \frac{Q}{C_o} = \frac{V_B}{R} \cdot \frac{d}{N^2} \cdot \frac{1}{C_o} \cdot \frac{(1-d)}{D} \cdot T \tag{20}$$

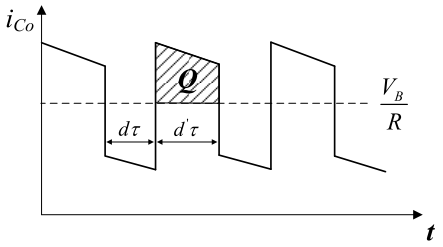

FIGURE 6. Capacitor current waveform to find voltage ripple using average charge.

In the interleaved converter, the current sharing ratio is proportionally reduced by the number of phases, so the magnetic field energy accumulated in each phase inductor is expressed as (21).

$$E_n = \sum_{k=1}^{n} \frac{1}{2} L_k \left(\frac{1}{N}\right)^2 \tag{21}$$

According to (21), the stored energy of the inductor is reduced by 1/8 times as much as the current sharing ratio of each phase is reduced by the 4-phase interleaved method. This has the effect of lowering inductance and inductor volume. In the non-isolated bidirectional converter of Fig. 5(a), Buck mode and Boost mode operate interlock. In this paper, only the step-down mode is described for the convenience of analysis. In step-down mode, the upper switches (T_{1A}, T_{3A}, T_{1B}, T_{3B}) become the main switches, and the lower switches (T_{2A}, T_{4A}, T_{2B}, T_{4B}) provide a freewheeling current path for the internal body diode. Fig. 5(b) shows the fundamental waveforms when the bidirectional dc-to-dc converter operates in step-down mode. The current flowing through the inductor of each phase rises during the switch's turn-on and falls during the turn-off. At this time, each phase current has a phase difference of 360/N degrees. In the step-down mode, as the upper switch is turned on, energy is accumulated in the inductors L_1, L_2, L_3, and L_4 and is discharged to the battery through the lower switches T_{2A}, T_{4A}, T_{2B}, and T_{4B}. At this time, the average voltage (v_L) across the inductor is the same as (22), and the relationship between the input/output voltage and the duty ratio is defined as (23).

$$v_L = v_B(1-D) - (V_{dc} - v_B) \cdot D \tag{22}$$

$$G_V = \frac{V_{dc}}{v_B} = D \tag{23}$$

1) STEADY-STATE ANALYSIS FOR THE CURRENT RISING SECTION OF THE INDUCTOR

Since the operation of all phases in the steady state is the same except for the phase difference of 360/N degrees, only one phase (L_1) is described for convenience of analysis. The relationship between the voltage across the inductor and the inductor current in the rising slope section in the step-down mode is shown in (24). Since the inductor voltage is equal to the difference between the battery voltage and the dc-link voltage, the slope of the current flowing through the inductor

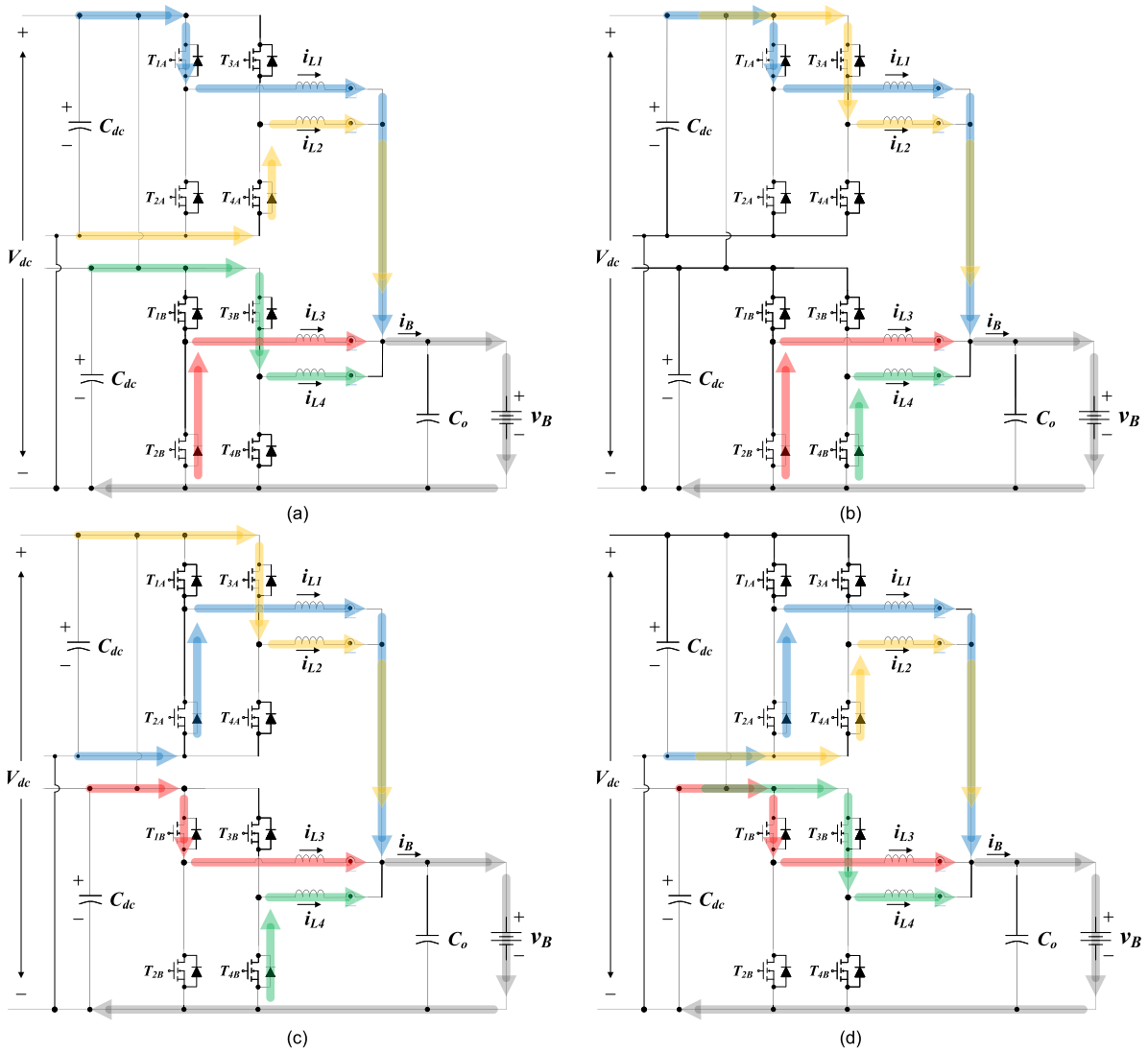

FIGURE 7. The behavior of the interleaved bidirectional dc-to-dc converter when charging the battery, (a) mode 1, $t_0 \sim t_1$, (b) mode 2, $t_1 \sim t_2$, (c) mode 3, $t_2 \sim t_3$, (d) mode 4, $t_3 \sim t_4$.

can be expressed as (25).

$$v_{L1} = L_1 \frac{di_{L1}}{dt} = v_B - V_{dc} \tag{24}$$

$$\frac{di_{L1}}{dt} = \frac{v_B - V_{dc}}{L_1} \tag{25}$$

In the steady state, if the initial current value of the inductor is an arbitrary minimum value (i_{L1min}), the inductor current during the turn-on period of the switch rises to the maximum value (i_{L1max}) at t=DT. Therefore, the maximum inductor current is expressed by (26), and the inductor current ripple equals (27).

$$i_{L1_{\max}} = i_{L1}(t = DT) = \frac{1}{L_1}\int_0^{DT} (v_B - V_{dc})\, dt + i_{L1_{\min}} \tag{26}$$

$$\Delta i_{L1} = i_{L1_{\max}} - i_{L1_{\min}} = \frac{v_B - V_{dc}}{L_1} \cdot DT \tag{27}$$

2) STEADY-STATE ANALYSIS FOR THE CURRENT FALLING SECTION OF THE INDUCTOR

The voltage across the inductor and the current slope in the section when the switch is turned off is as follows.

$$v_{L1} = L_1 \frac{di_{L1}}{dt} = -V_{dc} \tag{28}$$

$$\frac{di_{L1}}{dt} = -\frac{V_{dc}}{L_1} \tag{29}$$

While the switch is turned off, the inductor current falls from its maximum value (i_{L1max}) to its minimum value (i_{L1min}) at the point where t=T. At this time, the minimum current value of the inductor is (30), and the current ripple is expressed as (31).

$$i_{L1_{\min}} = i_{L1}(t = T) = \frac{1}{L_1}\int_{DT}^{T} -V_{dc} dt + i_{L1_{\max}} \tag{30}$$

$$\Delta i_{L1} = i_{L1_{\max}} - i_{L1_{\min}} = -\frac{V_{dc}}{L_1} \cdot (1 - D)\, T \tag{31}$$

C. DESIGN CONSIDERATION

The inductor should be designed considering the buck and boost modes in the proposed circuit configuration. In bidirectional operation, when the same load current in continuous current conduction mode (CCM) flows, the inductance of the inductor is generally set based on the buck, which requires a higher value. Table 1 shows the design specifications for one module among the proposed battery charging/discharging system circuit structures. The switching frequency is 40kHz, and the dc-link is boosted using the battery voltage in boost mode.

TABLE 1. Design specification for experiments.

Description	Value	Unit
Rated power capacity	8	kW (Each)
Battery voltage	0~150	V
Battery current	0~53.3	A
Input voltage (V_{dcH} + V_{dcL})	360~720	V
dc-link voltage (V_{dc})	180	V
dc-link current	~ 44.4	A
Switching frequency	40	kHz
Inductor	330	μH (Each)
Capacitor	1410	μF (470μF 3 parallel)

1) INDUCTOR DESIGN

When one 8kW module (2-phase interleaved) operates in buck mode, it is designed to work as CCM at 10% load current of the rated power capacity. The battery current corresponding to 5% of the rated power capacity is 2.67A, and the current flowing through the inductor of each phase becomes 1.33A.

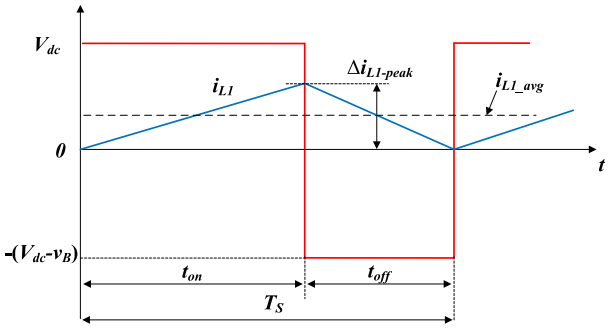

FIGURE 8. CCM (Continuous current Conduction Mode) and DCM (Discontinuous current Conduction Mode) boundary condition analysis.

When the dc-link voltage reaches the upper limit when operating in Buck mode, the duty ratio D is 0.83 by (23). And to operate the battery charging current corresponding to 5% of the rated power capacity in CCM mode, the minimum value of each phase inductor current is 1.33A.

$$L_1 \geq \frac{v_B\,(1-D)\cdot T_s}{2I_{L1\_avg}} \approx 235\mu H \tag{32}$$

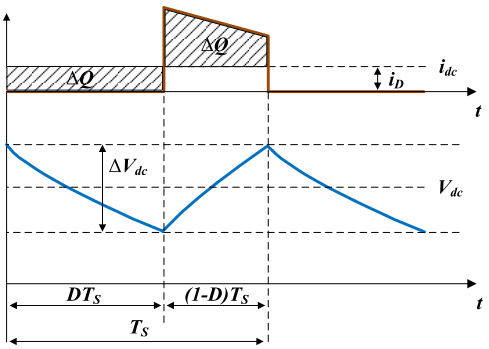

FIGURE 9. DC-link voltage ripple when operating in Boost mode.

The minimum inductance to satisfy CCM operation under the buck mode condition is 235μH. In the experiment, a value of 330μH, which is sufficiently more significant than the boundary value, is used to ensure complete CCM.

2) CAPACITOR DESIGN

Since the dc-link voltage ripple increases when operating in boost mode, the capacitance of the capacitor is selected based on the boost mode in Fig. 9.

In Boost mode, the duty ratio considering the step-up ratio of the battery voltage and the dc-link voltage is 0.167. Also, when operating at rated power capacity in Boost mode, R is 4.05 when obtained with a rated current of 44.4A for a dc-link voltage of 180V.

$$C_{dc} = \frac{DT_s}{R}\cdot\frac{V_{dc}}{\Delta v_{dc}} \approx 100\mu F \tag{33}$$

In (33), the dc-link voltage ripple was set to 1.8V, 1% of the dc-link voltage. Regarding voltage magnitude and stress, capacitors are generally selected up to 10 times larger. Three 470μF electrolytic capacitors were connected in parallel in the experiment, and 1410μF was selected.

3) CONTROLLER DESIGN

Fig. 10 shows the battery charge/discharge control block diagram. It consists of a current control unit, a voltage control unit, and a compensator. It is composed of a PI controller with anti-windup added to the voltage controller to prevent saturation of the controller when changing from CC mode to CV mode. In the battery charge/discharge system, a compensator is added to the current control loop to ensure a fast response to load fluctuations.

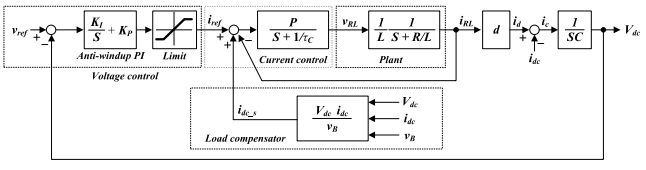

FIGURE 10. Battery CC-CV control block diagram.

Voltage sensing accuracy is critical in battery control. Suppose the error between the actual battery voltage and the measured battery voltage is about 1V. In that case, the CC mode can be controlled by the integrator of the battery charge/discharge controller, and an overcharge may occur in the battery. Methods such as a lookup table and curve fitting are widely used to compensate for the accuracy of the battery sensor voltage. In this paper, the low and high-voltage sections are divided and designed to reduce the voltage sensing error through curve fitting.

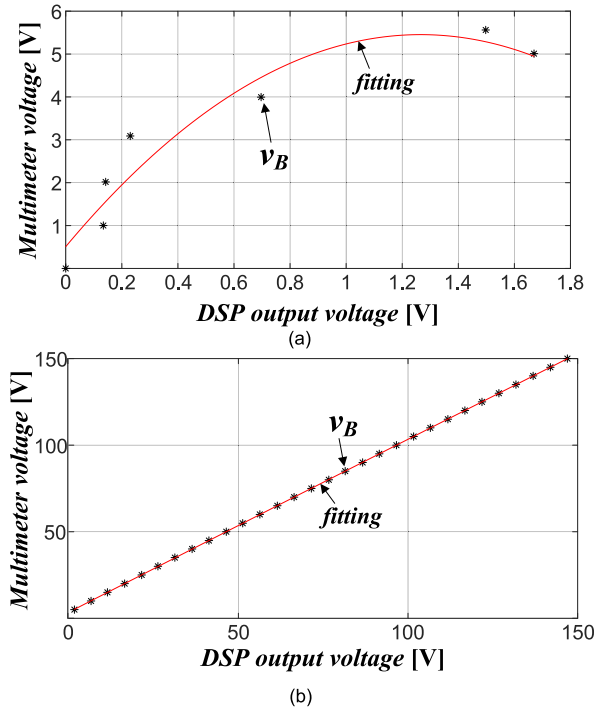

FIGURE 11. Battery measurement voltage compensation using curve fitting, (a) low voltage section, (b) high voltage section.

Fig. 11 is a quadratic function by MATLAB curve fitting to improve the accuracy of the battery-sensed voltage. A more accurate fitting value can be obtained in the low voltage section through a function higher than the quadratic function. Still, the low voltage section is 1.8V, which is not the charging/discharging region of the battery, so it is expressed as a quadratic function that can tolerate the error rate.

Table 2 compares the error rate between the measured voltage error and the actual voltage error. The curve fitting shows that the control error rate from 10V to 150V is up to 0.067%, and a precisely accurate sensing voltage performs control.

IV. SIMULATION AND EXPERIMENTAL RESULTS

In this chapter, the feasibility and superiority of the proposed battery charge/discharge circuit topology are verified through simulations and experiments using prototypes. In the proposed battery charging/discharging system, DAB has a significant purpose of electrical insulation with a proper voltage

TABLE 2. Comparison of battery voltage measurement error and control error.

Command voltage, V	Measurement voltage, V		Control error		Measured error	
	Instrument	DSP	V	%	V	%
10	9.98	10.004	-0.02	0.013	0.024	0.016
30	30	30.028	0	0	0.028	0.019
60	59.93	60.063	-0.07	0.047	0.133	0.089
90	90.1	90.124	0.1	0.067	0.024	0.016
120	120	119.999	0	0	-0.001	0.001
150	150	149.950	0	0	-0.05	0.033

ratio. The power delivery direction is determined by the dead time of the DAB switch and the voltage difference between the primary and secondary of the transformer. Fig. 12(a) shows that the DAB primary voltage phase precedes the secondary voltage phase, so power is transferred from the transformer primary to the secondary. In Fig. 12(b), since the voltage phase of the transformer's primary lags that of the secondary, power is transferred from the secondary to the primary. At this time, the magnitude of the inductor current is determined by the voltage across the transformer magnetizing inductance.

Fig. 13 is the simulation result of analyzing the voltage balancing characteristics for the case where the split capacitor's difference in capacitance and voltage connected in series to the DAB input side occurs in the proposed circuit structure. In Fig. 13(a), it can be confirmed that the voltages of the split capacitors are balanced after about 5ms even when the voltage difference between them is from 10% to 90%. However, when the voltage difference is 90%, the peak voltage due to the initial overshoot is about 550V and the primary current increases from about 40A to 150A. Suppose the peak voltage and current generated by the difference in the initial voltage of the capacitor is greater than the rated value of the capacitor or switch. In that case, there is a possibility of damage. Therefore, if a specific voltage difference or more occurs, a protection operation or an additional balancing operation is necessary. Fig. 13(b) is the simulation result for the case where the capacitance of the split capacitor connected in series to the input of DAB differs from 10% to 90%. Within 5ms after the overshoot, the split capacitors are voltage balanced. When the capacitance difference between the split capacitors is about 90%, the initial overshoot voltage and current generate peaks of about 440V and 100A. However, unlike Fig. 13(a), the overshoot continuously occurs due to the difference in capacitance, which causes continuous stress in the system.

Fig. 14 shows the simulation results of the split capacitor voltage and DAB current according to the difference in initial voltage and capacitance of the split capacitor. The maximum overshoot of the capacitor voltage generated by the difference in the initial voltage of the capacitor becomes higher than 500V, which is the working voltage of the capacitor,

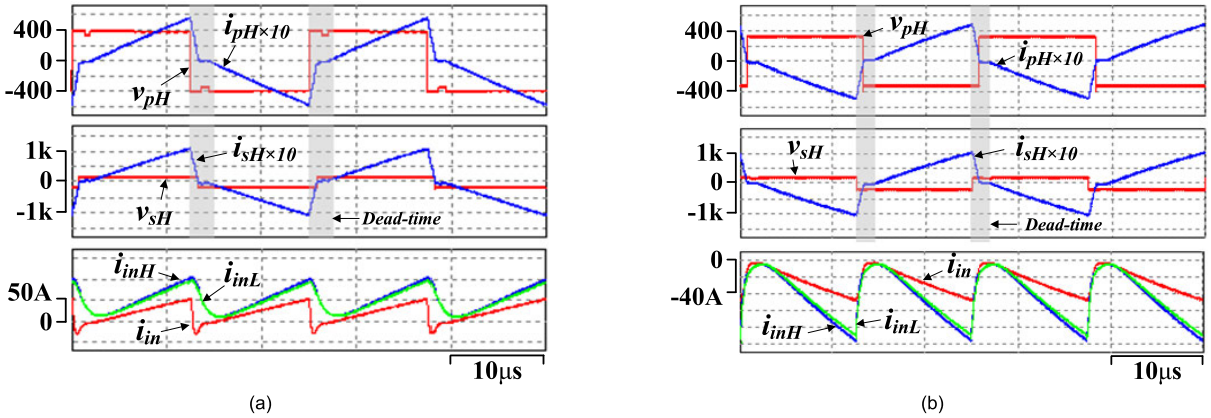

FIGURE 12. The operation of the DAB converter, according to the phase difference, (a) power transfer from the primary to the secondary, (b) power transfer from the secondary to the primary.

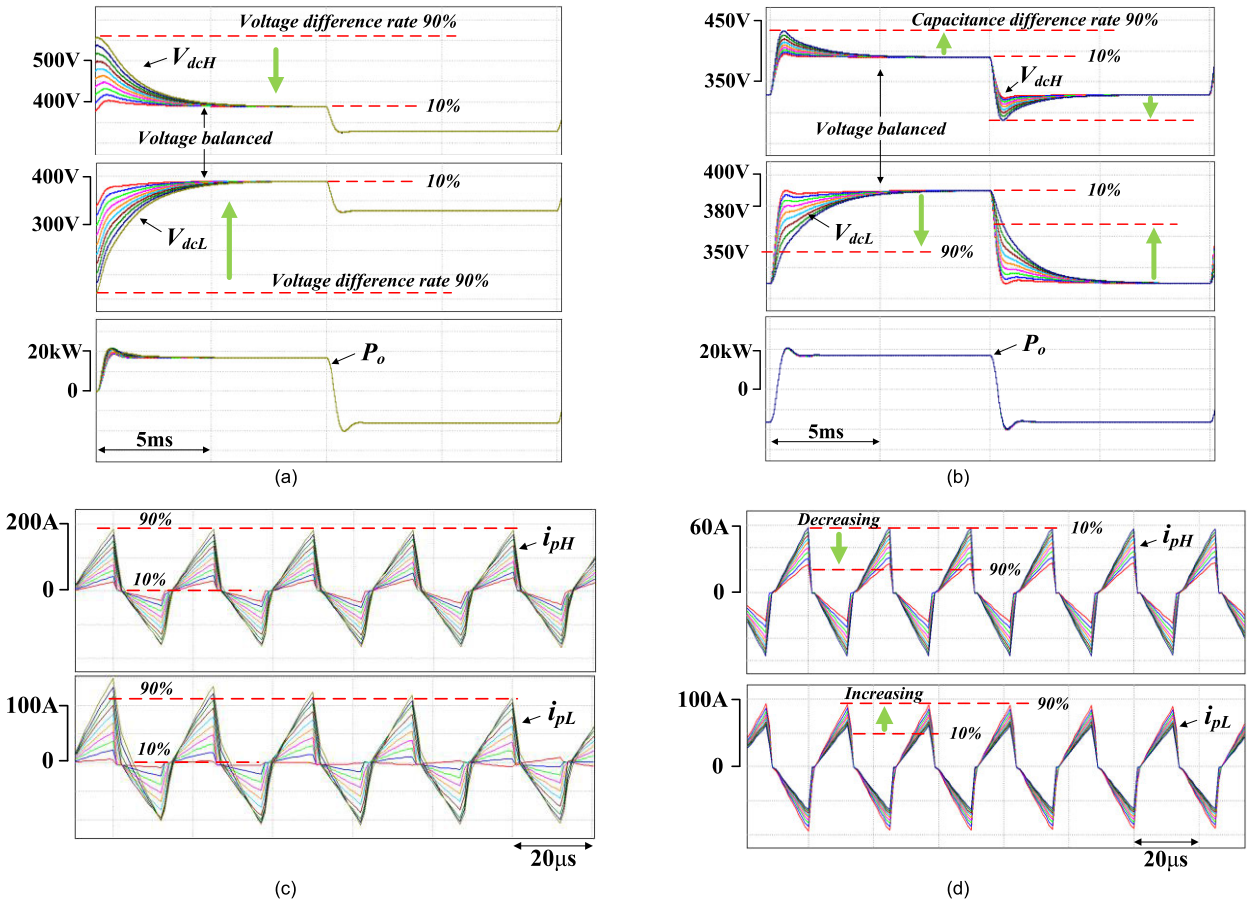

FIGURE 13. Voltage balancing characteristics when there is a difference in capacitance and voltage of the split capacitor connected in series to the DAB input side, (a) split capacitor voltage when the voltage difference between the split capacitors is 10% to 90%, (b) split capacitor voltage when the difference in the capacitance of the split capacitors is from 10% to 90%, (c) Primary current of upper and lower DAB converters under the same conditions as (a), (d) Primary current of upper and lower DAB converters under the same conditions as (b).

after about 70%. The primary current of both DAB modules increases constantly, and the magnitude of the current after 70% becomes about 100A or more. After about 70% of the voltage balancing due to the difference in capacitance, the upper module is 370V, and the lower module is 430V, resulting in a voltage difference of about 50V. The current also increases in proportion to the voltage.

Fig. 15 shows the simulation results of analyzing the characteristics of the converter output voltage change (changed to 25% from the rated load) according to the load variation. It is

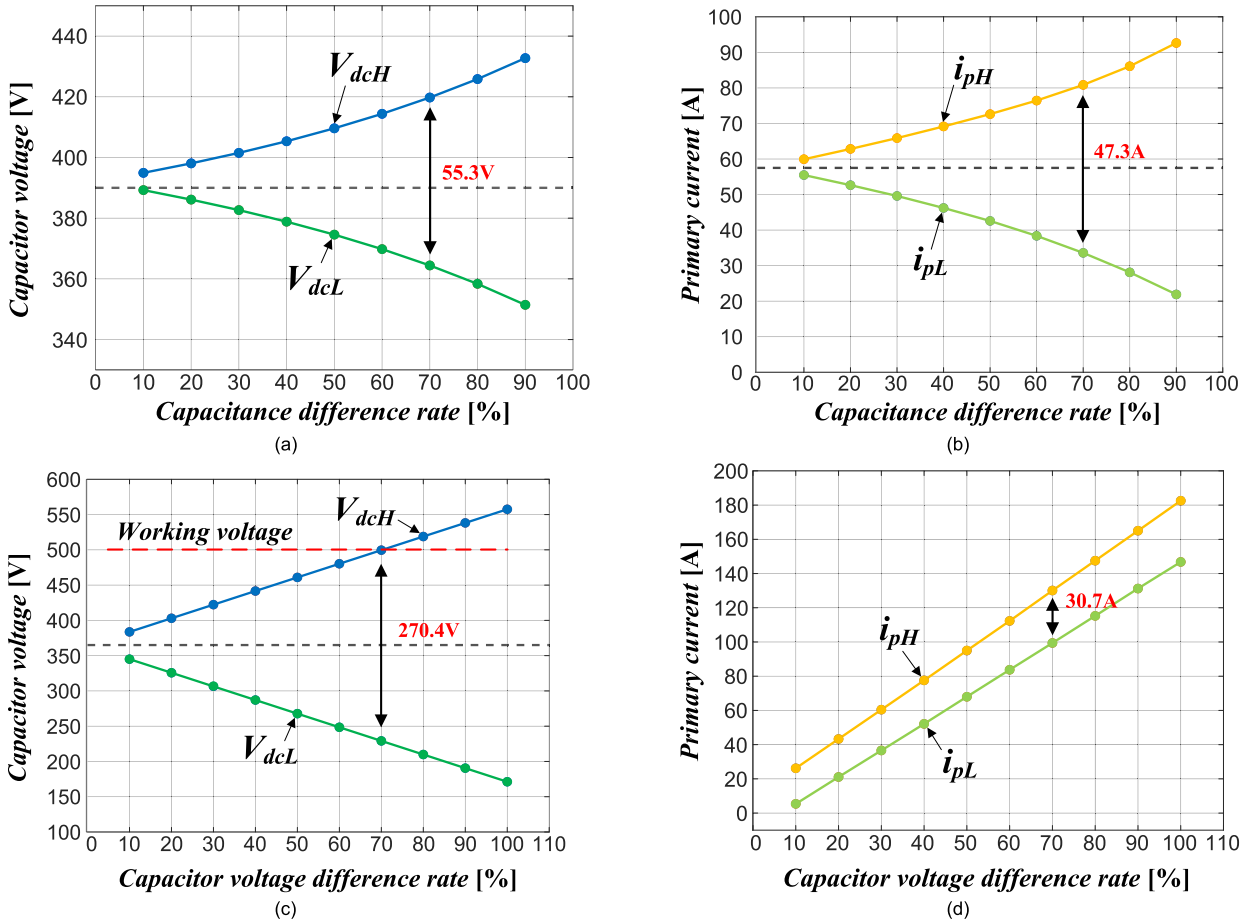

FIGURE 14. Split capacitor voltage and DAB current according to the difference in initial voltage and capacitance of the split capacitor, (a) split capacitor voltage according to the capacitance difference, (b) the upper and lower DAB primary current according to the capacitance difference, (c) split capacitor voltage according to the initial capacitor voltage, (d) the upper and lower DAB primary current according to the initial capacitor voltage.

the simulation result of switching from 8kW to 2kW and vice versa. At this time, the output voltage fluctuation appears as good as 10V.

Fig. 16 shows the prototype for the battery charge/discharge tester proposed in this paper. Two DABs and four non-isolated converters have an interleaved structure. An initial charging relay is added to prevent inrush current, and SMPS is used as a power source for the controller and relay operation. The controller used TI's TMS320F28377D and separately designed the sensing unit (CPU2) and the control unit (CPU1).

Fig. 17 shows the results of the operation experiment for the DAB used to secure a wide input voltage range and electrical insulation in the proposed approach. Since one module is designed as 8kW and the input voltage is 360V, in the case of a prototype in which two modules are combined, the 16kW input voltage can be operated at 720V. However, it was tested up to 5kW, considering the laboratory power supply conditions. Fig. 17(a) is the upper module's DAB primary and secondary voltage and current waveforms. The output voltage (input voltage of the non-isolated converter) is controlled to 150V. Fig. 17(a) is the experimental waveform before setting the switching angle so that the DAB switch current is flat. Therefore, the switch currents i_{pH} and i_{sH} are not flat current waveforms and the current peak increases as the load power capacity increases. Fig. 17(b) is an enlarged waveform at the turn-on moment of the DAB switch. From the primary and secondary voltages of the DAB, it can be seen that the phase of the primary voltage leads to the secondary voltage. Therefore, power is transferred from the primary to the secondary.

Fig. 18 shows the general operation waveform of the DAB converter when the load power capacity is increased to 500W, 1kW, 3kW, and 5kW. Each waveform is a primary-side voltage, secondary-side voltage, primary-side current, and secondary-side current waveform from top to bottom. The current peak becomes more significant as the magnitude of the power increases, and in particular, the current peak of the secondary is more significant than that of the primary.

Fig. 19 shows the operation waveform of the DAB converter after setting the switching angle so that the DAB switch current is flat. Each waveform is a primary-side voltage,

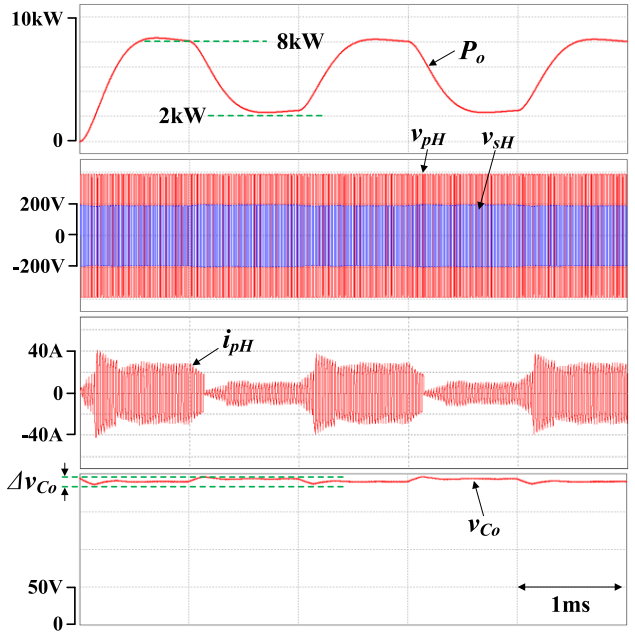

FIGURE 15. Simulation results of output voltage when the output load is changed from 8kW to 2kW and vice versa.

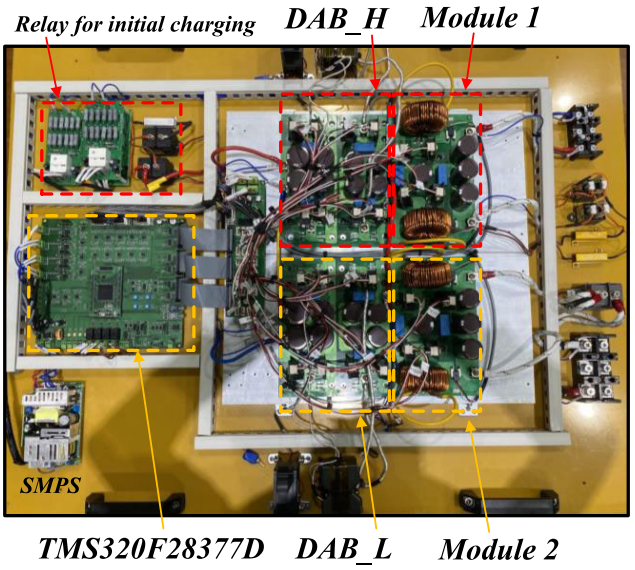

FIGURE 16. Prototype of the proposed battery charge/discharge tester.

secondary-side voltage, primary-side current, and secondary-side current waveform from top to bottom. Since the DAB switch current is controlled flat, it can be seen that the current peak does not increase significantly even when the load power capacity increases. Since the current peak is reduced, the conduction loss of the switch can be diminished, and the current rating of the switch can be reduced. In addition, since the phase difference of the voltage across the DAB is maintained not to be significant, it can be confirmed that the generation of reactive power due to the circulating current is small, so the loss due to the DAB is not significant.

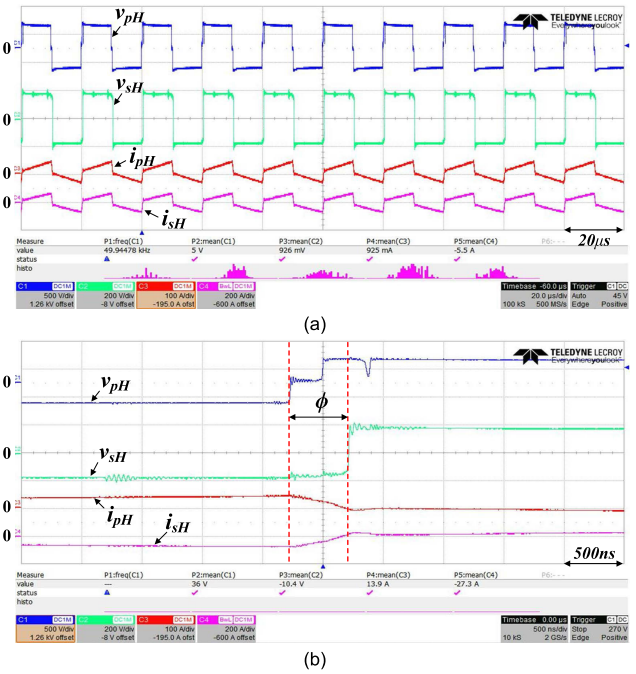

FIGURE 17. DAB operation in the proposed converter structure before setting the switching angle so that the DAB switch current is flat, (a) transformer primary voltage, secondary voltage, primary current, secondary current, from top to bottom, (b) Phase difference between primary and secondary voltages at DAB switch turn-on.

Fig. 20 is an experimental waveform that is soft-started by slowly decreasing the PWM dead time after charging the internal input capacitor through resistance and relay operation to prevent inrush current during the initial operation. Even with a soft-start function, the peak current is up to about 60A due to the large capacitance. It shows the stable operation in a steady state after the transient.

Fig. 21 shows the experimental waveform of response to load change. Fig. 21(a) is the experimental waveform when the load is changed from 100% load to 50% load. It shows stable response characteristics without overshooting. Fig. 21(b) is the test result waveform for voltage fluctuation. Even if you change the reference voltage from 150V to 100V, back to 150V, and then to 50V, you can see that the output voltage follows quickly.

Fig. 22 is an experimental waveform for analyzing the interleaved characteristics of the non-isolated converter. It can be seen that the 4-phase interleaved operation works with a 90-degree phase difference.

Fig. 23 is an experimental waveform to check the battery's charge/discharge response characteristics. A battery was modeled using a supercapacitor, and a charge/discharge system was implemented using a voltage controller and a current controller in the CV-CC controller loop. The target voltage was increased by about 10V to operate in CC mode, and it was confirmed through an experiment that the battery voltage reached nearly 90% and then worked in CV mode. When self-discharge is established by giving the battery a rest period, the voltage drop due to self-discharge is tiny.

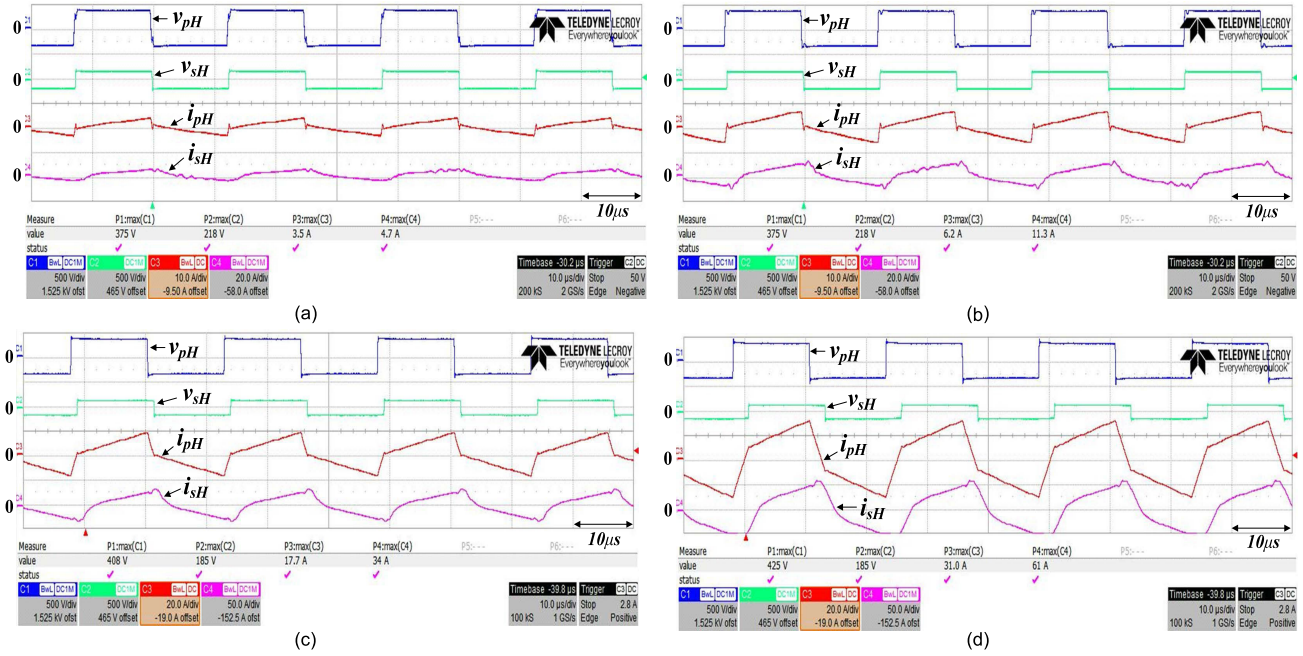

FIGURE 18. DAB operation according to the output power before setting the switching angle so that the DAB switch current is flat; primary voltage, secondary voltage, primary current, secondary current, from top to bottom, (a) 500W, (b) 1kW, (c) 3kW, (d) 5kW.

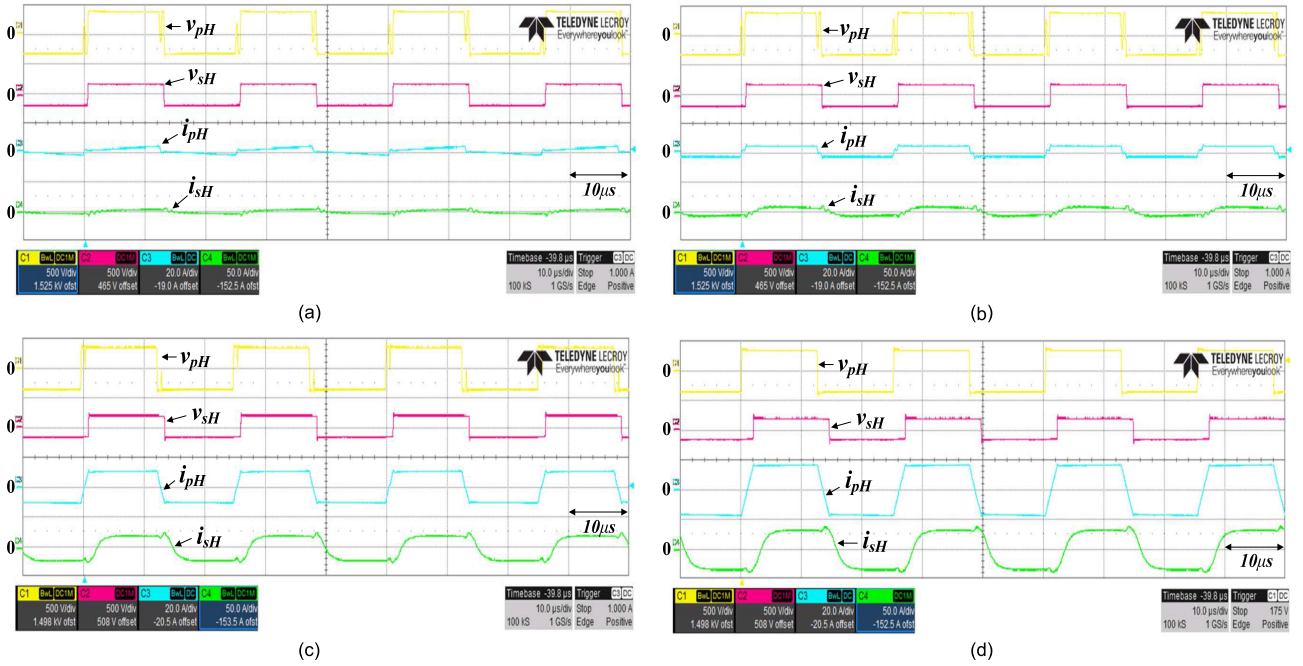

FIGURE 19. DAB operation according to the output power after setting the switching angle so that the DAB switch current is flat; primary voltage, secondary voltage, primary current, secondary current, from top to bottom, (a) 500W, (b) 1kW, (c) 3kW, (d) 5kW.

Fig. 24 shows the load variation test results of the proposed system. Even if there is a load change for 100A charging and discharging, the output current has a fast response characteristic within 2ms, and there is no voltage drop or overshoot voltage of the output voltage. This proves that the disturbance compensator of the charge/discharge controller works effectively.

Fig. 25 shows the ZVS region according to the DAB primary and secondary voltage ratio and phase difference ϕ in the proposed scheme. Since the voltage ratio M of the DAB

FIGURE 20. Starting characteristics of DAB converter with soft start function added in the proposed approach.

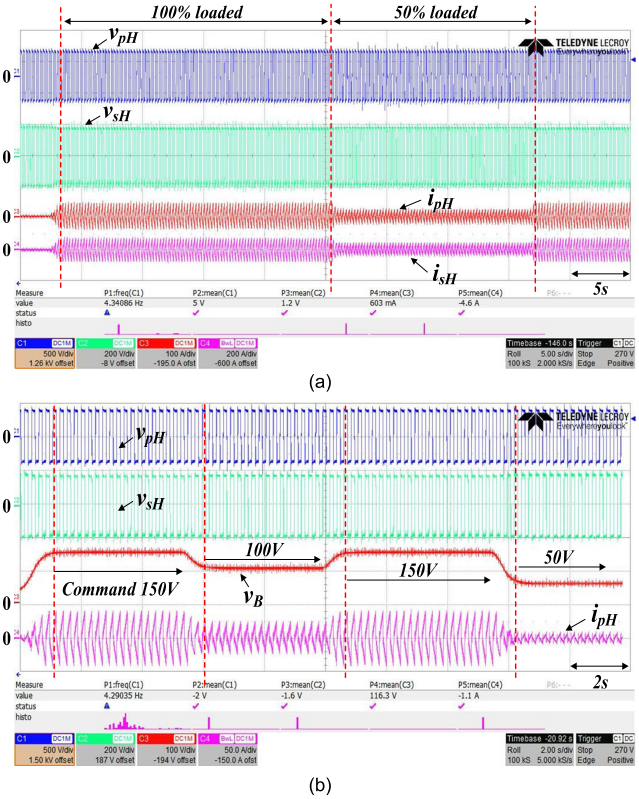

FIGURE 21. Starting and steady-state operation characteristics of DAB converter in the proposed system, (a) soft start applied to start characteristics, (b) steady-state operation.

converter is around 1, it shows that ZVS is possible in almost all load regions.

Fig. 26 shows four series-parallel structures for the proposed converter with wide input/output voltage ranges. The proposed converter circuit structure is modular and easy to expand. When input terminals are connected in series, the input voltage range can be increased, and when combined in parallel, input power capacity can be increased. Similarly, if the dc-link stages are connected in series, the range of the dc-link voltage can be increased, and when combined in parallel, the dc-link power capacity can be increased. What is

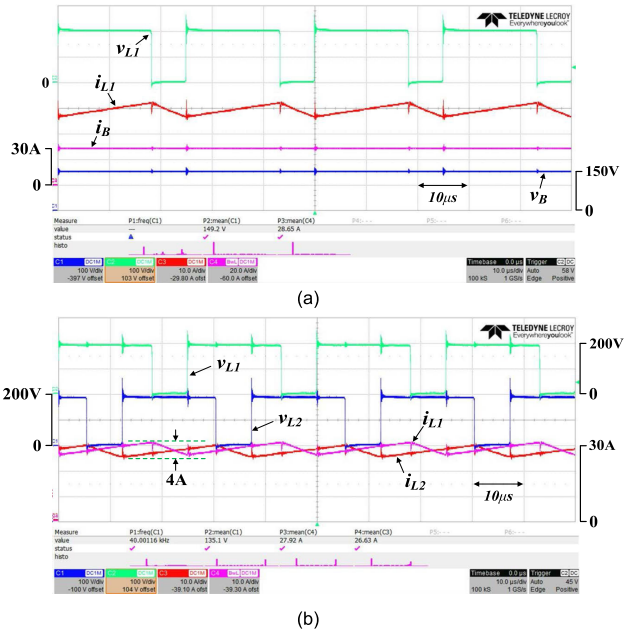

FIGURE 22. Interleaved behavior of output non-isolated converters, (a) The voltage across the inductor (L_1), inductor current, output current, (b) The voltage across DAB, inductor current for 2 phases of the 4 phase interleaved currents.

unique is that the input and output voltages of individual DAB converters are all the same regardless of the series-parallel structure. The voltage range increases with the series combination, and the power capacity rises only with the parallel combination. The output stage is composed of an interleaved non-isolated dc-dc converter, which can reduce current ripple as the module coupling increases.

Table 3 shows four series-parallel structures that can be created by combining two modules in the proposed converter. In Case 1, two input voltages are connected in series, and the dc-link stages are connected in parallel. In Case 2, two input voltages are connected in series, and the dc-link stages are also connected in series. In Case 3, two input voltages are connected in parallel; and the dc-link stages are also connected in parallel. In Case 4, two input voltages are connected in parallel, and the dc-link stages are connected in series. In all four cases, the actual input voltage applied to the individual DAB is 360V, and the dc-link voltage applied to the individual non-isolated dc-dc converter is 180V, which is the same. Therefore, the non-isolated dc-dc converter uses 180V as an input voltage to control the battery charging voltage in the range of 0 to 150V.

Fig. 27 compares the efficiency of the four series-parallel structures that can be created using the combination of two modules in the proposed converter. In the average efficiency for each case in Fig. 27(d), Case 1 shows the highest efficiency of 96.48% at 2kW load power capacity and the lowest efficiency of 93.118% at 5kW. The best efficiency is displayed in Case 3, and the highest efficiency was measured to be 96.8% at 1kW load power capacity, and the lowest

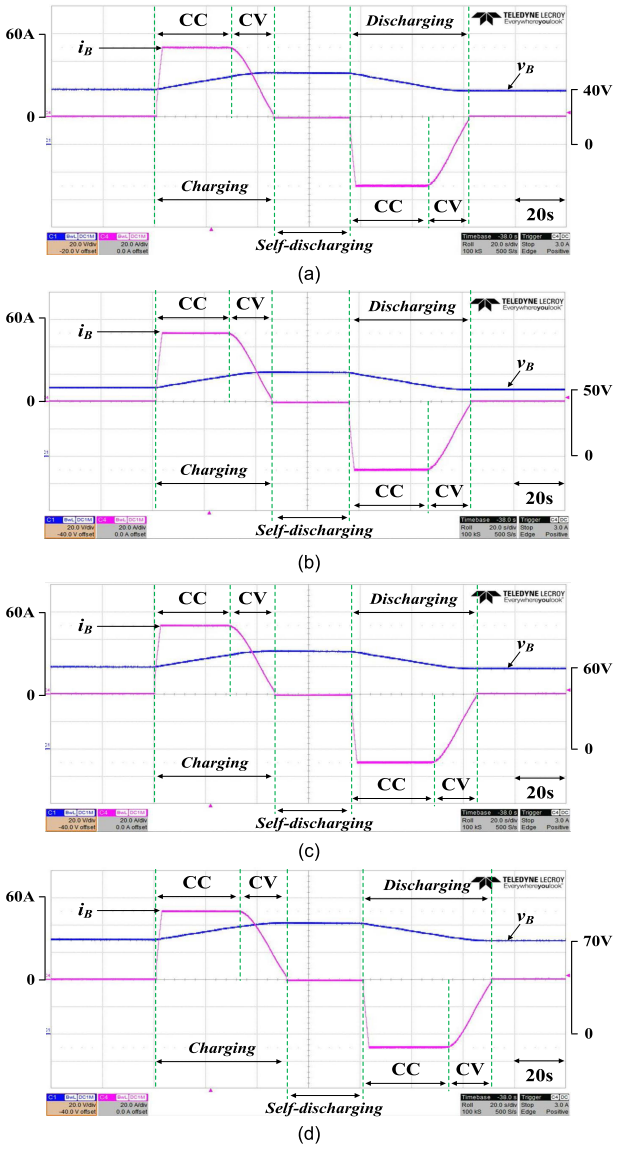

FIGURE 23. Battery charge/discharge test, (a) 50V charge, then discharge to 40V, (b) 60V charge, then discharge to 50V, (c) 70V charge, then discharge to 60V, (d) 80V charge, then discharge to 70V.

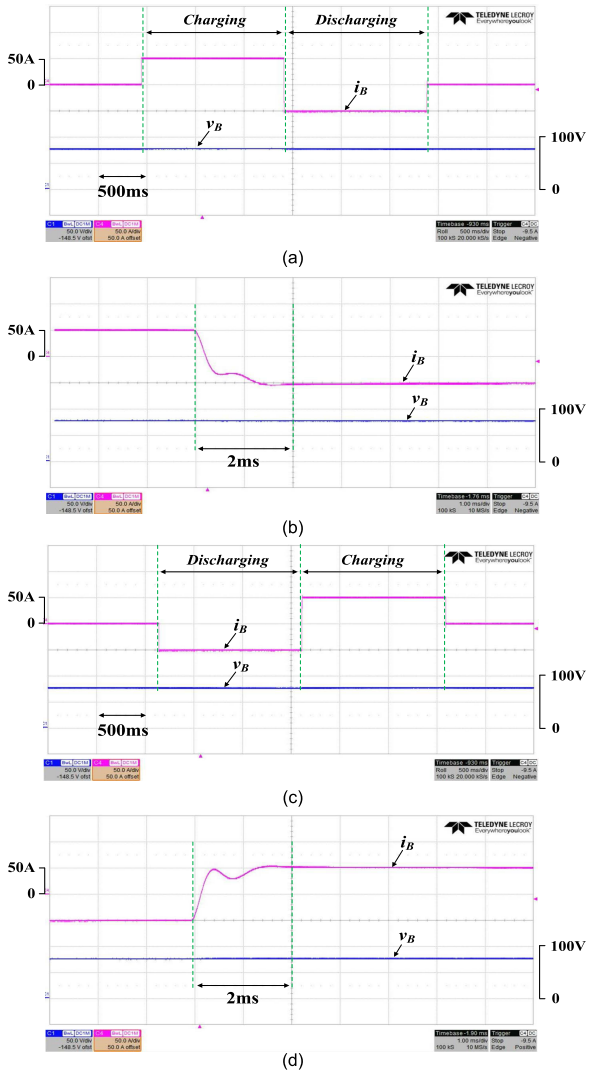

FIGURE 24. Response characteristics according to load fluctuations of the proposed system, (a) When changing from 100A charging to 100A discharging, (b) When changing from 100A discharge to 100A charge.

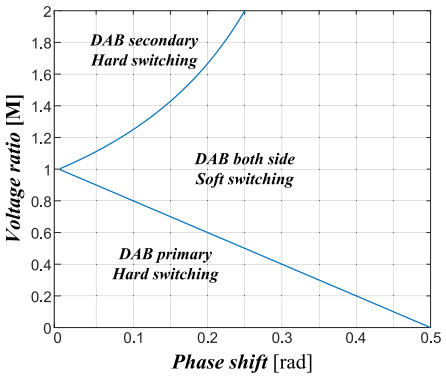

FIGURE 25. ZVS region according to DAB primary and secondary voltage ratio and phase difference ϕ in the proposed approach.

efficiency was measured to be 93.9% at 5kW. It can be judged as a result of Case 3 having a parallel structure in both input and dc-link. Overall, the average efficiency for all cases shows a difference of 1%. These results indicate that although the proposed converter can easily extend the input and output range through the module's series-parallel combination, the module series-parallel combination of the module does not significantly affect the efficiency because it operates in the form of a unit module.

Table 4 shows four circuit configurations that can be combined using two DAB converters. The voltage applied to each DAB is 360V regardless of the series or parallel combination of input voltages. If the outputs are parallel coupled, the output of each DAB must be equal to the battery charging voltage. When the output stage is series-coupled, the sum of the outputs of each DAB becomes equal to the battery charging voltage, so each DAB is output at half the battery voltage, and the sum of the two output voltages appears as

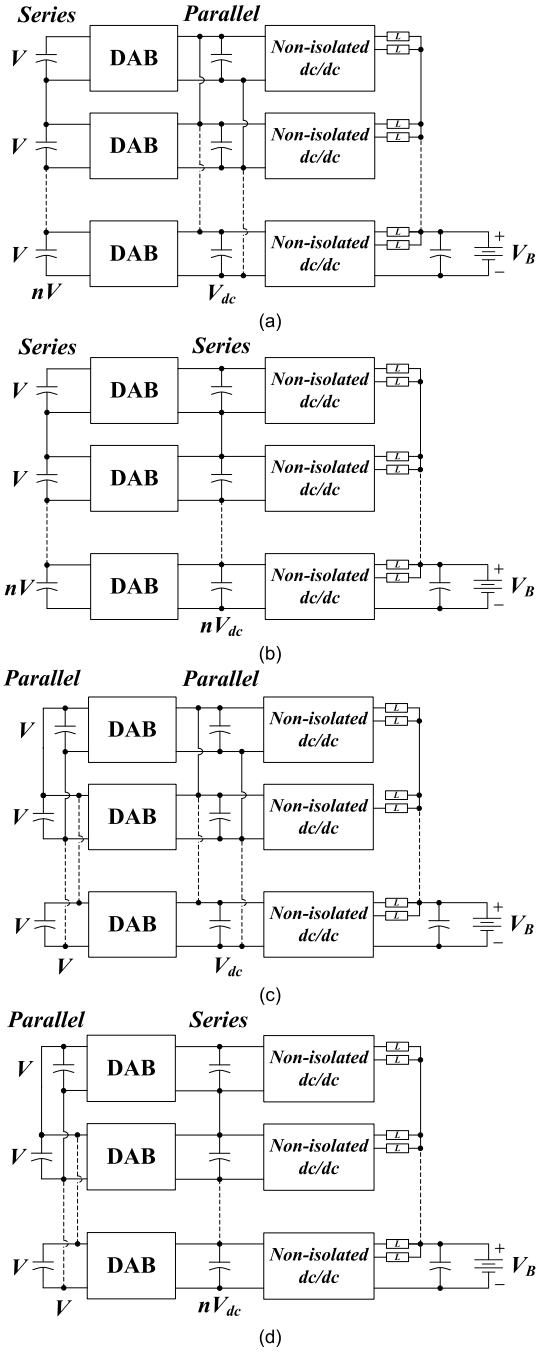

FIGURE 26. Series-parallel structure for the proposed converter to have a wide input/output voltage range, (a) the input terminal is connected in series, and the dc-link terminal is connected in parallel, (b) the input terminal is connected in series, and the dc-link terminal is also connected in series, (c) The input terminal is connected in parallel, and the dc-link terminal is also connected in parallel, (d) the input terminal is connected in parallel, and the dc-link terminal is connected in series.

TABLE 3. Four series-hyphenparallel structures that can be created by combining two modules in the proposed converter.

Case	Configuration	Description
1	Series Parallel; V, 2V, V_{dc}, V_B	Input V : V_{dc} : V_B 720V : 180V : (50~150)V @each DAB actual input voltage = 360V
2	Series Series; V, 2V, $2V_{dc}$, V_B	Input V : V_{dc} : V_B 720V : 360V : (50~150)V @each DAB actual input voltage = 360V actual dc-link voltage = 180V
3	Parallel Parallel; V, V, V_{dc}, V_B	Input V : V_{dc} : V_B 360V : 180V : (50~150)V
4	Parallel Series; V, V, $2V_{dc}$, V_B	Input V : V_{dc} : V_B 360V : 360V : (50~150)V @each DAB actual dc-link voltage = 180V

TABLE 4. Converter configuration using a series-parallel combination of two dab modules.

Case	Configuration	Description
I	Series Parallel; V, 2V, V_{dc}, V_B	Input V : V_{dc} : V_B 720V : (50~150)V : (50~150)V @each DAB actual input voltage = 360V
II	Series Series; V, 2V, $2V_{dc}$, V_B	Input V : V_{dc} : V_B 720V : (25~75)V : (50~150)V @each DAB actual input voltage = 360V V_{dc} is half of V_B
III	Parallel Parallel; V, V, V_{dc}, V_B	Input V : V_{dc} : V_B 360V : (50~150)V : (50~150)V
IV	Parallel Series; V, V, $2V_{dc}$, V_B	Input V : V_{dc} : V_B 360V : (25~75)V : (50~150)V V_{dc} is half of V_B

the battery charging voltage. Therefore, all four cases that can charge and discharge the battery using two DAB converters use 360V as input and generate a battery voltage of 50∼150V. Therefore, it can be equivalent to the condition that one DAB converter generates an output voltage of 50∼150V with an input voltage of 360V. The efficiency of generating output voltages of 50V, 100V, and 150V with one DAB converter module is measured and compared with the proposed converter.

As shown in Fig. 28(a), one DAB converter has the highest efficiency of 96.45% under the output voltage of 150V and 1kW generation and the lowest efficiency of 91.5% when

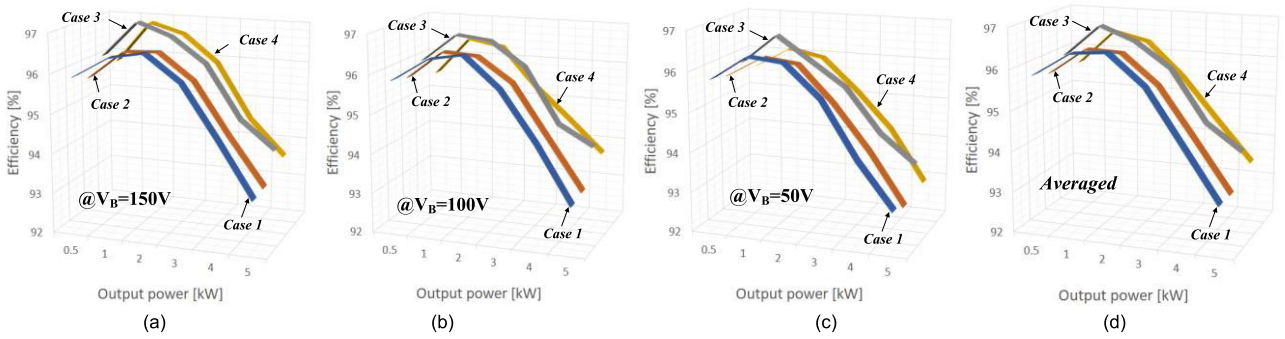

FIGURE 27. Efficiency comparison of the four series-parallel combination structures that can be created by combining two modules in the proposed converter, (a) Efficiency for each case according to power capacity at a battery charging voltage of 150V, (b) Efficiency for each case according to power capacity at a battery charging voltage of 100V, (c) Efficiency for each case according to power capacity at a battery charging voltage of 50V, (d) Average efficiency for each case when operating at 50∼150V.

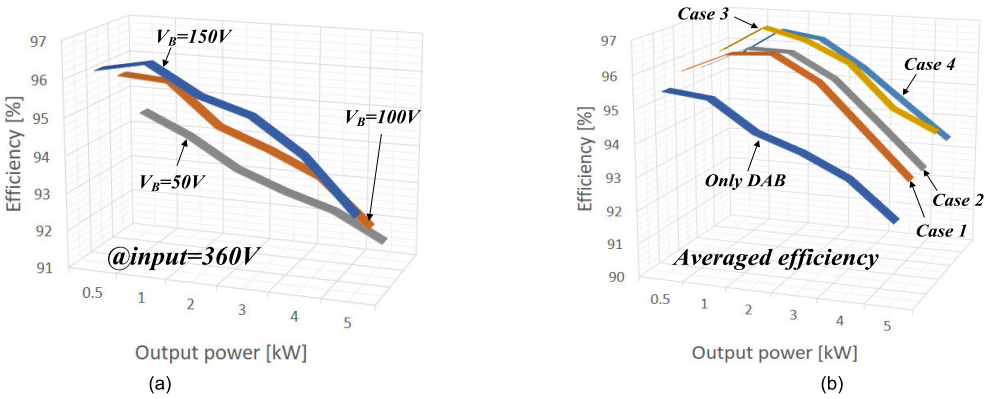

FIGURE 28. Comparison of the efficiency of the DAB converter and the proposed converter according to the load power capacity, (a) Efficiency when one DAB converter generates output voltages of 50V, 100V, and 150V from an input voltage of 360V, (b) Comparison of the average efficiency of each case of the proposed converter with the average efficiency of (a).

TABLE 5. Comparison of characteristics with similar methods employing dab converters.

Ref.	Modulation	Goal of optimization	ZVS range	RMS current	Output Power (kW, max)	Input Voltage (V)	Output Voltage (V)	Switching frequency (kHz)	Efficiency (%)
[54]	TPS	RMS current	Narrow	Low	1	200	160~230	20	95.8-98.2
[62]	TPS	RMS current + ZVS	Medium	Medium	1	200	200~400	50	76-95
[63]	APWM	RMS current	Narrow	High	0.5	380	42~56	50	86-95.5
[64]	APWM	RMS current	Narrow	High	0.625	200	50	50	76-95
[65]	AEPS +TPS	RMS current + ZVS	Wide	Low	5	380~420	40~56	50	93.7-97.7
Proposed (1 module)	SPS	RMS current + ZVS	Wide	Low	8	360~720	0~150	40	93.3-96.6

generating 50V and 5kW. This is because when the output voltage is high, the phase difference between both sides of the DAB is insignificant. Still, when the output voltage is low, the phase difference between both sides of the DAB is significant. Hence, the circulating current dramatically increases, and the loss increases due to the increase in reactive power. Fig. 28(b) shows the efficiency comparison result between the average value of Fig. 28(a) and the four possible combinations of the

proposed converter. One DAB converter shows relatively low efficiency by 1∼2% compared to the average efficiency of the four cases of the proposed method. In the case of the proposed method, the DAB can lower the peak of the operating current, the circulating current is small because the phase difference is not significant, and the switching loss is low due to soft switching. However, the switching loss increases as the load power capacity increases due to the hard switching of the non-isolated dc-dc converter. On the other hand, in the DAB converter, as the load power capacity increases, the DAB current peak increases proportionally to increase the conduction loss. When the output voltage is 50V, the phase difference of the DAB converter is more significant than when the output voltage is 150V, so the circulating current and reactive power increase accordingly, resulting in increased loss. In addition, since the output voltage control is also performed at the same time, a problem arises that the configuration of the controller becomes complicated.

Table 5 compares the characteristics of the proposed method with a similar approach using a DAB converter. The proposed converter connects the DAB converter and the non-isolated converter in series-parallel module form to ensure ZVS and have a wide input/output voltage range and to reduce the output ripple current with the interleaving structure. Regarding efficiency, [54] and [65] are the highest. However, it can be said that the proposed approach is the most excellent structure that has good efficiency characteristics and can cope with a wide input voltage and output voltage range.

V. CONCLUSION

We propose a converter structure for a battery charge/discharge tester that can respond to a wide input/output voltage range. The switching angle is controlled to minimize the circulating current and flatten the DAB current by keeping the minimum phase difference between the voltages at both ends of the DAB converter used for bidirectional power transfer and galvanic isolation. A non-isolated dc-to-dc converter is used to control the output voltage, and interleaved operation is used to reduce the output current ripple and improve the battery lifecycle.

The voltage balancing characteristics due to the difference between the initial voltage of the series-connected input capacitor and the capacitor capacity were analyzed, and design parameters were presented. The technical feasibility of the proposed system was verified through simulation and prototype experiments. As a result of the testing and measuring the efficiency of the battery charging and discharging of 50V∼150V under the condition that the proposed converter composes two modules in series and parallel, it showed good efficiency of 93.3∼96.6% and confirmed fast and stable response characteristics. Since the proposed circuit structure is easy to expand in a module, it will be suitable as a high-capacity battery charge/discharge tester with a wide input/output voltage range.

REFERENCES

[1] B. Zhao, Q. Song, W. Liu, and Y. Sun, "Overview of dual-active-bridge isolated bidirectional DC–DC converter for high-frequency-link power-conversion system," *IEEE Trans. Power Electron.*, vol. 29, no. 8, pp. 4091–4106, Aug. 2014.
[2] J. T. Kim, "Power circuit and controller design of DAB converter for battery charger," M.S. thesis, Dept. Elec. Eng., Pukyung Nat. Univ., Busan, South Korea, Feb. 2021.
[3] G. Gong, D. Hassler, and J. W. Kolar, "A comparative study of multicell amplifiers for AC-power-source applications," *IEEE Trans. Power Electron.*, vol. 26, no. 1, pp. 149–164, Jan. 2011.
[4] R. Ayyanar, R. Giri, and N. Mohan, "Active input–voltage and load–current sharing in input-series and output-parallel connected modular DC–DC converters using dynamic input-voltage reference scheme," *IEEE Trans. Power Electron.*, vol. 19, no. 6, pp. 1462–1473, Nov. 2004.
[5] J. Song-Manguelle and M. H. Todorovic, "A modular stacked DC transmission and distribution system for long distance subsea applications," *IEEE Trans. Ind. Appl.*, vol. 50, no. 5, pp. 3512–3524, Sep./Oct. 2014.
[6] J.-W. Kim, J.-S. Yon, and B. H. Cho, "Modeling, control, and design of input-series-output-parallel-connected converter for high-speed-train power system," *IEEE Trans. Ind. Electron.*, vol. 48, no. 3, pp. 536–544, Jun. 2001.
[7] T. Qian and B. Lehman, "Coupled input-series and output-parallel dual interleaved flyback converter for high input voltage application," *IEEE Trans. Power Electron.*, vol. 23, no. 1, pp. 88–95, Jan. 2008.
[8] T. Jin, K. Zhang, K. Zhang, and K. Smedley, "A new interleaved series input parallel output (ISIPO) forward converter with inherent demagnetizing features," *IEEE Trans. Power Electron.*, vol. 23, no. 2, pp. 888–895, Mar. 2008.
[9] V. Choudhary, E. Ledezma, R. Ayyanar, and R. M. Button, "Fault tolerant circuit topology and control method for input-series and output-parallel modular DC–DC converters," *IEEE Trans. Power Electron.*, vol. 23, no. 1, pp. 402–411, Jan. 2008.
[10] X. Ruan, W. Chen, L. Cheng, C. K. Tse, H. Yan, and T. Zhang, "Control strategy for input-series–output-parallel converters," *IEEE Trans. Ind. Electron.*, vol. 56, no. 4, pp. 1174–1185, Apr. 2009.
[11] P. Zumel, L. Ortega, A. Lazaro, C. Fernandez, A. Barrado, A. Rodriguez, and M. M. Hernando, "Modular dual-active bridge converter architecture," *IEEE Trans. Ind. Appl.*, vol. 52, no. 3, pp. 2444–2455, May 2016.
[12] N. Hou, P. Gunawardena, X. Wu, L. Ding, Y. Zhang, and Y. W. Li, "An input-oriented power sharing control scheme with fast-dynamic response for ISOP DAB DC–DC converter," *IEEE Trans. Power Electron.*, vol. 37, no. 6, pp. 6501–6510, Jun. 2022.
[13] N. Hou and Y. W. Li, "Overview and comparison of modulation and control strategies for a nonresonant single-phase dual-active-bridge DC–DC converter," *IEEE Trans. Power Electron.*, vol. 35, no. 3, pp. 3148–3172, Mar. 2020.
[14] R. W. A. A. De Doncker, D. M. Divan, and M. H. Kheraluwala, "A three-phase soft-switched high-power-density DC/DC converter for high-power applications," *IEEE Trans. Ind. Appl.*, vol. 27, no. 1, pp. 63–73, Feb. 1991.
[15] M. N. Kheraluwala, R. W. Gascoigne, D. M. Divan, and E. D. Baumann, "Performance characterization of a high-power dual active bridge DC-to-DC converter," *IEEE Trans. Ind. Appl.*, vol. 28, no. 6, pp. 1294–1301, Nov./Dec. 1992.
[16] F. Krismer and J. W. Kolar, "Accurate power loss model derivation of a high-current dual active bridge converter for an automotive application," *IEEE Trans. Ind. Electron.*, vol. 57, no. 3, pp. 881–891, Mar. 2010.
[17] F. Krismer, S. Round, and J. W. Kolar, "Performance optimization of a high current dual active bridge with a wide operating voltage range," in *Proc. 37th IEEE Power Electron. Spec. Conf.*, Jun. 2006, pp. 1–7.
[18] F. Krismer and J. W. Kolar, "Accurate small-signal model for the digital control of an automotive bidirectional dual active bridge," *IEEE Trans. Power Electron.*, vol. 24, no. 12, pp. 2756–2768, Dec. 2009.
[19] F. Krismer and J. W. Kolar, "Closed form solution for minimum conduction loss modulation of DAB converters," *IEEE Trans. Power Electron.*, vol. 27, no. 1, pp. 174–188, Jan. 2012.
[20] F. Krismer and J. W. Kolar, "Efficiency-optimized high-current dual active bridge converter for automotive applications," *IEEE Trans. Ind. Electron.*, vol. 59, no. 7, pp. 2745–2760, Jul. 2012.
[21] A. K. Tripathi, K. Mainali, D. C. Patel, A. Kadavelugu, S. Hazra, S. Bhattacharya, and K. Hatua, "Design considerations of a 15-kV SiC IGBT-based medium-voltage high-frequency isolated DC–DC converter," *IEEE Trans. Ind. Appl.*, vol. 51, no. 4, pp. 3284–3294, Jul. 2015.

[22] S. Poshtkouhi and O. Trescases, "Flyback mode for improved low-power efficiency in the dual-active-bridge converter for bidirectional PV microinverters with integrated storage," *IEEE Trans. Ind. Appl.*, vol. 51, no. 4, pp. 3316–3324, Jul. 2015.

[23] H. Akagi, T. Yamagishi, N. M. L. Tan, S.-I. Kinouchi, Y. Miyazaki, and M. Koyama, "Power-loss breakdown of a 750-V 100-kW 20-kHz bidirectional isolated DC–DC converter using SiC-MOSFET/SBD dual modules," *IEEE Trans. Ind. Appl.*, vol. 51, no. 1, pp. 420–428, Feb. 2015.

[24] A. R. Alonso, J. Sebastian, D. G. Lamar, M. M. Hernando, and A. Vazquez, "An overall study of a dual active bridge for bidirectional DC/DC conversion," in *Proc. IEEE Energy Convers. Congr. Exposit.*, Sep. 2010, pp. 1129–1135.

[25] R. T. Naayagi, A. J. Forsyth, and R. Shuttleworth, "Bidirectional control of a dual active bridge DC–DC converter for aerospace applications," *IET Power Electron.*, vol. 5, no. 7, pp. 1104–1118, Aug. 2012.

[26] G. Ortiz, J. Biela, D. Bortis, and J. W. Kolar, "1 Megawatt, 20 kHz, isolated, bidirectional 12kV to 1.2kV DC–DC converter for renewable energy applications," in *Proc. Int. Power Electron. Conf.*, Jun. 2010, pp. 3212–3219.

[27] H. Zhou and A. M. Khambadkone, "Hybrid modulation for dual-active-bridge bidirectional converter with extended power range for ultracapacitor application," *IEEE Trans. Ind. Appl.*, vol. 45, no. 4, pp. 1434–1442, Aug. 2009.

[28] J. W. Kolar, T. Friedli, F. Krismer, A. Looser, M. Schweizer, P. Steimer, and J. Bevirt, "Conceptualization and multi-objective optimization of the electric system of an airborne wind turbine," in *Proc. IEEE Int. Symp. Ind. Electron.*, Jun. 2011, pp. 32–55.

[29] R. Giri, V. Choudhary, R. Ayyanar, and N. Mohan, "Common-duty-ratio control of input-series connected modular DC–DC converters with active input voltage and load-current sharing," *IEEE Trans. Ind. Appl.*, vol. 42, no. 4, pp. 1101–1111, Jul. 2006.

[30] V. Choudhary, E. Ledezma, R. Ayyanar, and R. M. Button, "Fault tolerant circuit topology and control method for input-series and output-parallel modular DC–DC converters," *IEEE Trans. Power Electron.*, vol. 23, no. 1, pp. 402–411, Jan. 2008.

[31] W. Chen and G. Wang, "Decentralized voltage-sharing control strategy for fully modular input-series–output-series system with improved voltage regulation," *IEEE Trans. Ind. Electron.*, vol. 62, no. 5, pp. 2777–2787, May 2015.

[32] W. Chen, G. Wang, X. Ruan, W. Jiang, and W. Gu, "Wireless input-voltage-sharing control strategy for input-series output-parallel (ISOP) system based on positive output-voltage gradient method," *IEEE Trans. Ind. Electron.*, vol. 61, no. 11, pp. 6022–6030, Nov. 2014.

[33] G. Xu, D. Sha, and X. Liao, "Decentralized inverse-droop control for input-series–output-parallel DC–DC converters," *IEEE Trans. Power Electron.*, vol. 30, no. 9, pp. 4621–4625, Sep. 2015.

[34] L. Qu and D. Zhang, "Input voltage sharing control scheme for input series and output series DC/DC converters using paralleled MOSFETs," *IET Power Electron.*, vol. 11, no. 2, pp. 382–390, Feb. 2018.

[35] M. Abrehdari and M. Sarvi, "Comprehensive sharing control strategy for input-series output-parallel connected modular DC–DC converters," *IET Power Electron.*, vol. 12, no. 12, pp. 3105–3117, Oct. 2019.

[36] C. Luo and S. Huang, "Novel voltage balancing control strategy for dual-active-bridge input-series-output-parallel DC–DC converters," *IEEE Access*, vol. 8, pp. 103114–103123, 2020.

[37] L. Qu and D. Zhang, "Input voltage sharing control scheme for input series and output series DC/DC converters using paralleled MOSFETs," *IET Power Electron.*, vol. 11, no. 2, pp. 382–390, Feb. 2018.

[38] S. Inoue and H. Akagi, "A bi-directional isolated DC/DC converter as a core circuit of the next-generation medium-voltage power conversion system," in *Proc. 37th IEEE Power Electron. Spec. Conf.*, Jun. 2006, pp. 18–22.

[39] S. Falcones, X. Mao, and R. Ayyanar, "Topology comparison for solid state transformer implementation," in *Proc. IEEE PES Gen. Meeting*, Minneapolis, MN, USA, Jul. 2010, pp. 25–29.

[40] R. Redl, L. Balogh, and D. W. Edwards, "Optimum ZVS full-bridge DC/DC converter with PWM phase-shift control: Analysis, design considerations, and experimental results," in *Proc. IEEE Appl. Power Electron. Conf. Expo. (ASPEC)*, Orlando, FL, USA, Feb. 1994, pp. 13–17.

[41] X. Ruan and B. Li, "Zero-voltage and zero-current-switching PWM hybrid full-bridge three-level converter," *IEEE Trans. Ind. Electron.*, vol. 52, no. 1, pp. 2213–2220, Feb. 2005.

[42] H. J. Chiu and L. W. Lin, "Zero-voltage and zero-current-switching PWM hybrid full-bridge three-level converter," *IEEE Trans. Ind. Electron.*, vol. 52, no. 3, pp. 709–718, Jun. 2005.

[43] W. J. Lee, C. E. Kim, G. W. Moon, and S. K. Han, "A new phase-shifted full-bridge converter with voltage-doubler-type rectifier for high-efficiency PDP sustaining power module," *IEEE Trans. Ind. Electron.*, vol. 55, no. 6, pp. 2450–2458, Jun. 2008.

[44] B. Yang, F. C. Lee, A. J. Zhang, and G. Huang, "LLC resonant converter for front end DC/DC conversion," in *Proc. 17th Annu. IEEE Appl. Power Electron. Conf. Expo.*, Dallas, TX, USA, Mar. 2002, pp. 10–14.

[45] Y. Gu, Z. Lu, L. Hang, Z. Qian, and G. Huang, "Three-level LLC series resonant DC/DC converter," *IEEE Trans. Power Electron.*, vol. 20, no. 4, pp. 781–789, Jul. 2005.

[46] F. Musavi, M. Craciun, D. S. Gautam, W. Eberle, and W. G. Dunford, "An LLC resonant DC–DC converter for wide output voltage range battery charging applications," *IEEE Trans. Power Electron.*, vol. 28, no. 12, pp. 5437–5445, Dec. 2013.

[47] R. W. A. A. De Doncker, D. M. Divan, and M. H. Kheraluwala, "A three-phase soft-switched high-power-density DC/DC converter for high-power applications," *IEEE Trans. Ind. Appl.*, vol. 27, no. 1, pp. 63–73, Jan. 1991.

[48] N. Schibli, "Symmetrical multilevel converters with two quadrant DC–DC feeding," Ph.D. dissertation, Ecole Polytechnique Federale de Lausanne, Lausanne, France, 2000.

[49] B. Zhao, Q. Song, W. Liu, and Y. Sun, "Overview of dual-active-bridge isolated bidirectional DC–DC converter for high-frequency-link power-conversion system," *IEEE Trans. Power Electron.*, vol. 29, no. 8, pp. 4091–4106, Aug. 2014.

[50] S. Inoue and H. Akagi, "A bidirectional DC–DC converter for an energy storage system with galvanic isolation," *IEEE Trans. Power Electron.*, vol. 22, no. 6, pp. 2299–2306, Nov. 2007.

[51] G. G. Oggier, G. O. García, and A. R. Oliva, "Modulation strategy to operate the dual active bridge DC–DC converter under soft switching in the whole operating range," *IEEE Trans. Power Electron.*, vol. 26, no. 4, pp. 1228–1236, Apr. 2011.

[52] B. Zhao, Q. Song, and W. Liu, "Efficiency characterization and optimization of isolated bidirectional DC–DC converter based on dual-phase-shift control for DC distribution application," *IEEE Trans. Power Electron.*, vol. 28, no. 4, pp. 1711–1727, Apr. 2013.

[53] J. Li, Q. Luo, D. Mou, Y. Wei, and X. Zhang, "Comprehensive optimization modulation scheme of low current level and wide ZVS range for dual active bridge converter with dead-zone control," *IEEE Trans. Power Electron.*, vol. 37, no. 3, pp. 2731–2748, Mar. 2022.

[54] A. Tong, L. Hang, G. Li, X. Jiang, and S. Gao, "Modeling and analysis of a dual-active-bridge-isolated bidirectional DC/DC converter to minimize RMS current with whole operating range," *IEEE Trans. Power Electron.*, vol. 33, no. 6, pp. 5302–5316, Jun. 2018.

[55] N. Hou, W. Song, and M. Wu, "Minimum-current-stress scheme of dual active bridge DC–DC converter with unified phase-shift control," *IEEE Trans. Power Electron.*, vol. 31, no. 12, pp. 8552–8561, Dec. 2016.

[56] J. Guo, H. Han, G. Xu, Z. Cai, H. Wang, Y. Sun, and M. Su, "Design considerations for PPS controlled current-fed DAB converter to achieve full load range ZVS and low inductor current stress," *IEEE Trans. Ind. Appl.*, vol. 57, no. 6, pp. 6261–6276, Nov. 2021.

[57] S. Bal, D. B. Yelaverthi, A. K. Rathore, and D. Srinivasan, "Improved modulation strategy using dual phase shift modulation for active commutated current-fed dual active bridge," *IEEE Trans. Power Electron.*, vol. 33, no. 9, pp. 7359–7375, Sep. 2018.

[58] X. Pan, H. Li, Y. Liu, T. Zhao, C. Ju, and A. K. Rathore, "An overview and comprehensive comparative evaluation of current-fed-isolated-bidirectional DC/DC converter," *IEEE Trans. Power Electron.*, vol. 35, no. 3, pp. 2737–2763, Mar. 2020.

[59] F. Z. Peng, H. Li, G.-J. Su, and J. S. Lawler, "A new ZVS bidirectional DC–DC converter for fuel cell and battery application," *IEEE Trans. Power Electron.*, vol. 19, no. 1, pp. 54–65, Jan. 2004.

[60] H. Xiao and S. Xie, "A ZVS bidirectional DC–DC converter with phase-shift plus PWM control scheme," *IEEE Trans. Power Electron.*, vol. 23, no. 2, pp. 813–823, Jun. 2008.

[61] Q. Gu, L. Yuan, J. Nie, J. Sun, and Z. Zhao, "Current stress minimization of dual-active-bridge DC–DC converter within the whole operating range," *IEEE J. Emerg. Sel. Topics Power Electron.*, vol. 7, no. 1, pp. 129–142, Mar. 2019.

[62] W. Choi, K.-M. Rho, and B.-H. Cho, "Fundamental duty modulation of dual-active-bridge converter for wide-range operation," *IEEE Trans. Power Electron.*, vol. 31, no. 6, pp. 4048–4064, Jun. 2016.
[63] E. L. Carvalho, C. A. Felipe, L. V. Bellinaso, C. M. D. O. Stein, R. Cardoso, and L. Michels, "Asymmetrical-PWM DAB converter with extended ZVS/ZCS range and reduced circulating current for ESS applications," *IEEE Trans. Power Electron.*, vol. 36, no. 11, pp. 12990–13001, Nov. 2021.
[64] S. Chakraborty and S. Chattopadhyay, "Fully ZVS, minimum RMS current operation of the dual-active half-bridge converter using closed-loop three-degree-of-freedom control," *IEEE Trans. Power Electron.*, vol. 33, no. 12, pp. 10188–10199, Dec. 2018.
[65] M. Mahdavifard, N. Mazloum, F. Zahin, A. KhakparvarYazdi, A. Abasian, and S. A. Khajehoddin, "An asymmetrical DAB converter modulation and control systems to extend the ZVS range and improve efficiency," *IEEE Trans. Power Electron.*, vol. 37, no. 10, pp. 12774–12792, Oct. 2022.

SUNG-JUN PARK received the B.S., M.S., and Ph.D. degrees in electrical engineering and the Ph.D. degree in mechanical engineering from Pusan National University, Busan, South Korea, in 1991, 1993, 1996, and 2002, respectively. From 1996 to 2000, he was an Assistant Professor with the Department of Electrical Engineering, Koje College, Koje, South Korea. From 2000 to 2003, he was an Assistant Professor with the Department of Electrical Engineering, Tongmyong College, Busan. Since 2003, he has been a Professor with the Department of Electrical Engineering, Chonnam National University, Gwangju, South Korea. From 2007 to 2013, he was the Head of the Energy Power Center of Samsung Electro-Mechanics. From 2018 to 2020, he worked as the CEO of G&EPS. His research interests include renewable energy, ESS, electric vehicle-related converters and inverters, power conversion devices, motor driver design and control, battery charge/discharge converter, wireless charging and energy economics, trend prediction, and statistical data analysis. He is a member of the KIEE, KIPE, and KIIEE. Since 2019, he has been serving as the President of the Korean Society of Industry Convergence.

JIN WOOK PARK received the B.S. degree in electronics engineering from Mokpo National Maritime University, in 2011, and the M.S. degree in electrical engineering from Chonnam National University, in 2015, where he is currently pursuing the Ph.D. degree in electrical engineering. His research interests include power electronics, including design and control of power converters for dc grid, multilevel inverters for photovoltaic systems, and battery charger for electric vehicle.

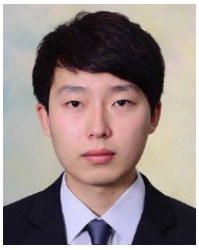

KUK HYEON KIM received the B.S. degree in mechatronics engineering from Chosun University, in 2017, and the M.S. degree in electrical engineering from Chonnam National University, in 2019, where he is currently pursuing the Ph.D. degree in electrical engineering. His research interests include power electronics, including design and control of power converters for dc grid, multilevel inverters for photovoltaic systems, and battery charger for electric vehicle.

FEEL-SOON KANG (Member, IEEE) received the B.S. degree in electrical engineering from Gyeongsang National University, Jinju, South Korea, in 1998, and the M.S. and Ph.D. degrees in electrical engineering from Pusan National University, South Korea, in 2000 and 2003, respectively. Since 2003, he has been a Postdoctoral Fellow with the Department of Electrical Engineering, Osaka University, Japan. From 2004 to 2022, he was a Professor with the Department of Electronic Engineering, Hanbat National University, Daejeon, South Korea. Since 2022, he has been a Professor with the Department of Mechatronics Engineering, Gyeongsang National University. His research interests include power electronics, including the design, control, and reliability analysis of various power conversion systems for photovoltaic power generation, electric vehicles, and HVDC systems. He is a member of KIEE and KIPE. He received the Student Award and Best Presentation Prizes from the IEEE Industrial Electronics Society, in 2001, and he was honored with Academic Awards from Pusan National University and Hanbat National University, in 2003 and 2005, respectively. He also received several Best Paper Awards from The Korean Institute of Electrical Engineers (KIEE) and The Korean Institute of Power Electronics (KIPE). He served as the Vice-Chairman of the Organizing Committee for the International Telecommunications Energy Conference (IEEE Intelec 2009), IEEE Vehicle Power and Propulsion Conference (IEEE VPPC 2012), IEEE Transportation Electrification Conference and Expo (IEEE ITEC 2016), and International Conference on Electrical Machines and Systems (ICEMS 2010, 2013, and 2018), and as a Secretary of International Conference on Magnetically Levitated Systems and Linear Drives (Maglev 2011). He served as an Associate Editor for the IEEE TRANSACTIONS ON INDUSTRIAL ELECTRONICS, from 2004 to 2011.